Mon. Not. R. astr. Soc. (1987) **227**, 403–451

Non-thermal pair production in compact X-ray sources: first-order Compton cascades in soft radiation fields

Roland Svensson *NORDITA, Blegdamsvej 17, DK-2100 Copenhagen Ø, Denmark*

Accepted 1987 February 23. Received 1987 February 16; in original form 1986 December 15

Summary. Non-thermal pair cascades, where injected relativistic electrons (or pairs) cool by inverse Compton scattering on soft photons in the Thomson limit and where the resulting hard photons pair produce on other up-scattered photons, are described by an integral equation. A general integral equation for *all* relevant optical depths is obtained by using a simple prescription for the radiative transfer effects due to photon–photon absorption and to Compton scattering by the cooled pairs.

The integral equation is solved analytically in the limit of large injection compactness L_i/R (L_i is the injected particle power and R the size of the injection region), where every γ-ray photon produces a pair (*saturated* pair production). Each photon generation is described separately and has a well-determined spectral index at small photon energies, being $\alpha = \frac{1}{2}$ and $\frac{3}{4}$ for the first and second generation, respectively.

Analytical and numerical solutions of the general integral equation show how reprocessing by the pair cascade becomes increasingly important with increasing injection compactness and how the saturated limit is approached. The efficiency of converting injected power into pair rest mass can reach levels of about 10 per cent. Solutions close to the Klein–Nishina limit show extreme sharp transitions to pair dominated states as L_i/R increases past $2\times10^{29}\,\mathrm{erg\,s^{-1}\,cm^{-1}}$.

A parameter space study shows that the observed 'universal' X-ray index, 0.7, and the observed (almost universal) 2–10 keV compactness in Seyfert galaxies are obtained for unsaturated cascades with a pair Thomson depth of a few tenths. Radiation pressure effects may be responsible in limiting the Thomson depth of pair cascade clouds to be less than unity. Feedback mechanisms causing rapid variability are briefly discussed.

1 Introduction

The radiation from active galactic nuclei has a non-thermal character as the power emitted per logarithmic bandwidth is approximately constant over several decades in photon energy ranging from the infrared up to hard X-rays. In objects with large optical polarization (BL Lacs and

OVVs) the emission is most likely due to non-thermal relativistic electrons emitting synchrotron radiation in large-scale magnetic fields. Although much of the radiation in objects with small optical polarization may be reprocessed primary power, there is no reason to believe that injected non-thermal relativistic electrons are not responsible for part of the photon emission. The hard X-ray and soft γ-ray emission, in particular, are extremely difficult to account for using thermal mechanisms as no known process can maintain a thermal particle distribution at the necessary temperatures. If most primary power is injected as non-thermal electrons with large Lorentz factors, γ, then most of the photon power can easily be radiated as γ-rays at photon energies, ε (in units of mc^2, where m is the electron rest mass and c the speed of light), larger than unity. Photons at energy ε may produce electron–positron pairs by interacting with target photons of energy $>\varepsilon^{-1}$. Jelley (1966) emphasized the possibility that high-energy γ-rays may pair produce on the numerous target photons rather than escape in compact sources. Herterich (1974) noted that the target luminosity to size ratio, L/R, of a compact object is the factor determining whether a high-energy photon will get absorbed or not. Cavaliére & Morrison (1980) found that when L/R is large enough injected electrons (or positrons) Compton cool on the radiation field before they escape the injection region. Guilbert, Fabian & Rees (1983) defined the dimensionless parameter

$$\ell = \frac{L}{R}\frac{\sigma_{\mathrm{T}}}{mc^3}, \tag{1.1}$$

(σ_{T} is the Thomson cross-section), which more recently has been called the *compactness* parameter. The condition in Herterich (1974) that the absorption optical depth to photon–photon pair production is larger than unity approximately becomes (assuming most photon power to be near mc^2)

$$\tau_{\gamma\gamma} \approx \ell/4\pi > 1, \tag{1.2}$$

i.e. $\ell > 10$ for absorption to be important. The ratio of the Compton cooling time to the escape time, R/c, in the Cavaliere–Morrison argument is, similarly, written in terms of the compactness as $\approx(\ell\gamma)^{-1}$ and $\ell > 1$ is a sufficient condition for cooling to dominate escape at all Lorentz factors.

Within black hole models for compact objects (for reviews, see Phinney 1983; Begelman, Blandford & Rees 1984; Rees 1984) the definition of the compactness parameter can be rewritten as

$$\ell = \frac{2\pi}{3}\left(\frac{L}{L_{\mathrm{Edd}}}\right)\left(\frac{3R_g}{R}\right), \tag{1.3}$$

where $L_{\mathrm{Edd}} = 2\pi m_{\mathrm{p}} c^3 R_g/\sigma_{\mathrm{T}}$ is the pair-free Eddington luminosity, R_g is the Schwarzschild radius, and m_{p} the proton rest mass. The condition for ample pair production is easily satisfied in models having a luminosity larger than a few per cent of the Eddington limit coming from a region within some $10R_g$. The density of produced pairs, n_+, may dominate the density of ionization electrons, n_{i}, in accreting plasma changing, e.g. cooling rates and the influence of radiation pressure. If an energy $em_{\mathrm{p}}c^2$ per accreted proton is dissipated (with e being the efficiency) and if a fraction x, the pair yield, of the non-thermal luminosity, L_{NT}, is converted into pair rest mass, then the pair particle to ion ratio becomes

$$\frac{2n_+}{n_{\mathrm{i}}} = e\left(\frac{m_{\mathrm{p}}}{m}\right)x\left(\frac{L_{\mathrm{NT}}}{L}\right) \approx 18\left(\frac{e}{0.1}\right)\left(\frac{x}{0.1}\right)\left(\frac{L_{\mathrm{NT}}}{L}\right). \tag{1.4}$$

For characteristic accretion efficiencies ($e \approx 0.06$–0.42) and for maximum pair yields ($x \approx 10$ per cent, to be shown in Section 3.3) this ratio is easily greater than unity unless L_{NT}/L is small. In the

relatively ion-free disc funnels and coronas, non-thermally produced pairs may dominate even more.

Bonometto & Rees (1971) realized that non-thermal pair production would initiate a pair cascade of alternating photon–photon *pair* production ($\gamma\gamma \rightarrow e^+e^-$) and *photon* production through inverse Compton scattering of soft photons ($\gamma e \rightarrow \gamma e$). The pair cascade redistributes the injected power making the secondary photon and pair injection approach a state where equal power is injected per logarithmic bandwidth. Guilbert *et al.* (1983) outlined the pair cascade scenario discussing most of the physical effects expected to be involved. Most importantly they showed that the cooled secondary pairs easily can have a Thomson depth $\tau_T \approx (x\ell)^{1/2}$ larger than unity, adding the complicating possibility that the cool pairs could reprocess the non-thermal photons through thermal Comptonization. The work since then on non-thermal pair production has been based on some variant of the Guilbert *et al.* scenario. In general, the models consider a uniform region of size R, where a primary particle power L_i is injected at Lorentz factors less then or equal to some γ_{max}, and where a soft photon power L_s is injected at some photon energy $\varepsilon_s \ll 1$ (or where the energy density of virtual magnetic field photons is $B^2/8\pi$). The aim is then to self-consistently solve the particle and photon kinetic equations together with the radiative transfer in order to find how the effects of power redistribution through pair cascades and thermal Comptonization affect the emerging photon spectrum for increasing compactness $\ell_i \propto L_i/R$ at different ratios of L_i/L_s (or L_i/cR^2B^2). The cloud is assumed to be steady and static and any injected pairs cool and annihilate on the spot. The injected particle power is converted to escaping radiation with some fraction x, the pair yield, becoming pair rest mass before eventually escaping as annihilation photons.

It is important to emphasize two differences between pair cascades occurring in compact radiation fields (where $\gamma\gamma \rightarrow e^+e^-$ produces the pairs) and those occurring in the strong B-fields of pulsars (where photo-magnetic pair production dominates) or in the matter dominated atmospheres of planets and stars (where photon–particle pair production dominates). The first difference concerns spatial structures. In the two latter cases the structure of the cascade medium is often easily specified. The spatial structure of a radiation field as a cascade medium must, on the other hand, be solved for using the radiative transfer equation. The cascade may modify the radiation field through various opacity effects and, furthermore, radiation produced by the cascade itself may add a dominant contribution at photon energies where few non-cascade photons are injected. The latter is always the case for cascades where $\gamma_{max}\varepsilon_s < 1$ (see Section 2) as then the target photons in the photon–photon interactions are produced by the cascade. The *non-linearity* this introduces is characteristic of cascades in radiation fields. The second difference concerns isotropy. Atmospheric or pulsar cascade showers are highly anisotropic as the particle injection occurs non-uniformly and anisotropically. Pair cascades in compact radiation fields, however, are expected to have a much larger degree of isotropy. In accretion scenarios for active galactic nuclei the particle injection is thought to occur at many sites simultaneously throughout the injection region (*cf.* Guilbert *et al.* 1983) and the merging of cascade showers from many injection sites makes the photon and pair distributions rather isotropic and uniform.

Pair cascades in soft (meaning $\varepsilon \ll 1$) radiation fields can be classified into three groups according to the degree of non-linearity involved.

(i) *Fully linear cascades.* Here both the photon and the pair production takes place on the external soft radiation field at ε_s (that also could be virtual magnetic field photons). For the soft photons at ε_s to be up-scattered to pair producing energies $> \varepsilon_s^{-1}$ requires $\gamma_{max}\varepsilon_s > 1$. Furthermore, ℓ_s must be larger than ~ 10 for significant pair production to take place on the soft photons, while $\ell_i < 10$ is necessary for pair production not to take take place on the soft ($\varepsilon < 1$) cascade photons.

Table 1.

Author(s)	Luminosity ratio	Injection compactness	Injection type	Cascade type
External soft photons				
Bonometto & Rees (1971)	$L_i/L_s>1$	$\ell_i\gg10$	Mono-energetic	III
Aharonian, Vardanian & Kirillov-Ugryumov (1984)	$L_i/L_s<1$	$\ell_i<10$	Power law, $\Gamma=2$	I
Aharonian & Vardanian (1985)				
Aharonian *et al.* (1985)				
Kazanas (1984)	$L_i/L_s<1$	$\ell_i\gg10$	Power law, $\Gamma<2$	II
Zdziarski & Lightman (1985)	$L_i/L_s<1$	$\ell_i<20$	Mono-energetic	II
Fabian *et al.* (1986)	$0.1<L_i/L_s<10$	$\ell_i>4$	Mono-energetic	III
Kardashev *et al.* (1986)	$L_i/L_s>1$	–	Mono-energetic	III
Zdziarski & Lamb (1986)	$L_i/L_s>1$	Any ℓ_i	Power law, $\Gamma>2$	III
Svensson (this work)	$L_i/L_s<1$	Any ℓ_i	Mono-energetic	II
Virtual magnetic photons (synchrotron self-Compton)				
Stern (1985), Novikov & Stern (1986)	$L_i/cR^2B^2>1$	–	Mono-energetic	III
Zdziarski (1986)	$L_i/cR^2B^2=1$	$\ell_i=20$–150	Power law, $\Gamma>2$	III
Ghisellini (1987)	$L_i/cR^2B^2<1$	$\ell_i\gg10$	Mono-energetic	II

(ii) *Partly non-linear cascades.* When the compactness of the soft ($\varepsilon<1$) cascade radiation is large enough ($\ell_i>10$) pair production by γ-ray photons at $\varepsilon<\varepsilon_s^{-1}$ will take place on the cascade photons making the cascade partially non-linear.

(iii) *Fully non-linear cascades.* When the energy density of the soft cascade radiation is larger than the energy density of the soft background photons (i.e. $L_i>L_s$) then photon production of γ-rays may dominantly be caused by pairs scattering (and cooling) on the soft cascade photons. *Both* photon and pair production take place on the soft cascade photons making the cascade completely non-linear.

Table 1 classifies some recent work on pair cascades in 'isotropic' soft radiation fields. Small-angle cascade showers of type I in anisotropic radiation fields were treated by Burns & Lovelace (1982) and Lovelace & Ruchti (1983). Almost every work in Table 1 differs in the basic assumptions made, a fact not always appreciated when comparisons of results have been made.

Even though most work has made major simplifying assumptions concerning radiative transfer, the photon kinetic equation had to be solved numerically. This has made it difficult to understand and to quantify the detailed mechanisms causing, e.g. the shape of the resulting photon spectra, the magnitude of the pair yield, and the behaviour of the transition to a situation dominated by secondary pairs. Here we attempt to reach such an understanding mostly by analytical means. To avoid the large number of generations in type I cascades, where, furthermore, the interactions take place in the Klein–Nishina limit, this work only considers the case $\gamma_{max}\varepsilon_s<1$. Also to avoid the full non-linearity of type III cascades only the case $L_i/L_s<1$ is considered. Previous work treating the case L_i/L_s and $\gamma_{max}\varepsilon_s<1$ (i.e. type II cascades) are those by Kazanas (1984), Zdziarski & Lightman (1985, hereafter ZL85), and Fabian *et al.* (1986, hereafter F86). Kazanas (1984) converted the steady photon (or pair) kinetic equation into an integral equation solving it approximately for the steady pair distribution in the limit $\ell_i\gg10$. Besides giving a more reasonable description of the radiative transfer ZL85 wrote the integral equation in a very convenient form and solved it analytically for the escaping photon spectrum in the limit $\ell_i\ll1$ and numerically in the range up to $\ell_i\approx20$ at which point the Thomson depth of cool pairs becomes larger than unity requiring thermal Comptonization to be taken into account. F86

solved the time-dependent photon kinetic equation for both steady and non-steady injection at $\ell_i > 4$ and covered the regime $0.1 < L_i/L_s < 10$ where higher order Compton scatterings (i.e. up-scattering of the first-order cascade photons) becomes important. Here it is even more difficult to disentangle the various effects responsible for the numerical results.

We adopt the approach of ZL85. To be able to cover all values of ℓ_i their formalism is extended to include the effects of thermal Comptonization (i.e. down-scattering by cold pairs) in an approximate way. The paper is organized as follows. A study of parameter space (ε_s, γ_{max}) in Section 2 shows where pair cascades due to first-order Compton scattered photons occur. Then the general integral equation describing the cascade together with the two expressions for the optical depths due to Thomson scattering and photon–photon pair production are derived. Radiative transfer effects are either prescribed (down-scattering) or treated using a simple escape probability (photon–photon absorption). Emphasis is on the injected pair and photon spectra rather than on the actual spectral density distributions as the injection spectra are more fundamental (*cf.* emissivity versus the intensity in stellar radiative transfer). The spectral photon density distribution depends on the details of the radiative transfer while the injection spectra become independent of the radiative transfer in the optically thick case when every γ-ray photon produces a pair (*saturated* pair production). In Section 3 the integral equation for saturated pair production is solved analytically for any type of particle injection. The cases of mono-energetic and power-law injection are then considered. The transition from unsaturated to saturated pair production is discussed in Section 4 for mono-energetic particle injection. Analytical and numerical solutions of the integral equation show how opacity and pair production feedbacks always cause a transition to a fully pair-dominated situation near $\ell_i \approx 1$–5. The pair yields and the emerging spectra including a number of additional spectral features due to annihilation photons are also calculated. Section 5 considers the results of previous work on first-order Compton cascades. In Section 6 the observed X-ray properties of active galactic nuclei are discussed in the context of pair cascade models. Some extensions of the present work are outlined in Section 7. A summary of the main results concludes the paper.

A few appendices contain details on the photon kinetic equation, on necessary rates of non-thermal and thermal processes, on the analytical solution for saturated pair cascades, and on the effects of second-order Compton scatterings.

Many of the relevant results presented here were summarized in a non-technical manner in Svensson (1986). After the completion of the present paper a preprint by Lightman & Zdziarski (1987) was received. They extend the theory of pair cascades further and numerically solve the kinetic equations for any L_i/L_s as well as for power law injection of particles.

2 Pair cascades in fix soft photon backgrounds

2.1 PARAMETER SPACE OF PAIR CASCADES

Consider a spherical region of size R, where a luminosity L_i is injected uniformly as relativistic particles extending up to a maximum Lorentz factor $\gamma_{max} \gg 1$. In the same region a soft photon luminosity L_s is injected at the dimensionless photon energy (in units of mc^2) $\varepsilon_s \ll 1$. The injected particles cool by (inverse Compton) scattering the soft photons at ε_s giving rise to a steady particle spectrum $N(\gamma)\,\mathrm{cm}^{-3}$, and to a Compton scattered photon spectrum extending from ε_s up to an approximate maximum photon energy

$$\varepsilon_{max,1} = \max[\tfrac{4}{3}\gamma_{max}^2 \varepsilon_s, \gamma_{max}] \tag{2.1}$$

for scatterings in the Thomson and Klein–Nishina limit, respectively. Limiting our study to scatterings in the Thomson limit requires $\gamma_{max}\varepsilon_s < \tfrac{3}{4}$. As a large fraction of the injected

particle luminosity may emerge as photon luminosity at $\varepsilon<1$, a sufficient requirement for the soft photons at ε_s to dominate the cooling is simply $L_s \gg L_i$.

If the optical depth to photon–photon pair production at energy $\varepsilon \gg 1$ is large enough, then a photon injected at ε will not escape but rather interact with a photon of energy $>1/\varepsilon$ to produce an electron–positron pair, each particle having an energy $\varepsilon/2$ (see Appendix B2), with the pair spectrum extending up to $\gamma_{\max,1}=\varepsilon_{\max,1}/2$. The injected pairs Thomson cool on the soft photons at ε_s, giving rise to a second generation of Compton scattered photons extending up to

$$\varepsilon_{\max,2}=\tfrac{4}{3}(\gamma_{\max,1})^2\varepsilon_s=2\gamma_{\max}^4(\tfrac{2}{3}\varepsilon_s)^3. \tag{2.2}$$

If $\varepsilon_{\max,2}>2$ then a second pair generation is injected that Compton scatters further photons. The pair cascade continues until the last Compton scattered photon generation has a too small maximum energy to make further pairs. The maximum photon energy of the kth photon generation is

$$\varepsilon_{\max,k}=2\gamma_{\max}^{2^k}(\tfrac{2}{3}\varepsilon_s)^{2^k-1} \tag{2.3a}$$

with the corresponding maximum Lorentz factor of the kth pair generation being

$$\gamma_{\max,k}=\gamma_{\max}^{2^k}(\tfrac{2}{3}\varepsilon_s)^{2^k-1}. \tag{2.3b}$$

Obvious recursive relations are (ZL85) $\varepsilon_{\max,k+1}=\varepsilon_{\max,k}^2\varepsilon_s/3$ and $\gamma_{\max,k+1}=2\gamma_{\max,k}^2\varepsilon_s/3$. The condition to have k secondary pair generations and $k+1$ photon generations becomes

$$\gamma_{\max}>(\tfrac{2}{3}\varepsilon_s)^{-(1-2^{-k})}. \tag{2.4}$$

The number of secondary pair generations for given $\gamma_{\max}$ and ε_s is

$$K=\mathrm{Int}\left[\frac{\log(\log\tfrac{2}{3}\varepsilon_s/\log\tfrac{2}{3}\gamma_{\max}\varepsilon_s)}{\log 2}\right]. \tag{2.5}$$

Fig. 1 shows how parameter space (ε_s, $\gamma_{\max}$) can be divided into a number of regions. The Thomson condition $\gamma_{\max}\varepsilon_s=\tfrac{3}{4}$ (diagonal solid line) divides parameter space to two main regions, one where the pair cascade takes place in the Klein–Nishina limit (Klein–Nishina cascades) and the other one where at least the first-order Compton scatterings are in the Thomson limit (Thomson cascades). Condition (2.4) for $k=2, 3, 4$ outline the regions (dashed lines) where there are 2, 3 and 4 pair generations caused by first-order Compton scattered photons. When the maximum photon energy of first-order Compton scattered photons $\varepsilon_{1C}\equiv\varepsilon_{\max,1}<2$ or, equivalently,

$$\gamma_{\max}<(\tfrac{2}{3}\varepsilon_s)^{-1/2} \tag{2.6}$$

then no pairs can be generated by first-order photons. However, second-order Compton scattered photons can produce pairs as long as their maximum energy $\varepsilon_{2C}=(\tfrac{4}{3})\gamma_{\max}^2\varepsilon_{1C}>2$ or, equivalently,

$$\gamma_{\max}>(\tfrac{8}{9}\varepsilon_s)^{-1/4}. \tag{2.7}$$

Similarly, for

$$\gamma_{\max}>(\tfrac{32}{27}\varepsilon_s)^{-1/6} \tag{2.8}$$

third-order Compton scattered photons can produce pairs. These regions are also shown by the solid lines in Fig. 1. In this paper we are concerned with Thomson cascades mediated by first-order Compton scattered photons only. Particular cases considered here lie on the fat horizontal line in Fig. 1.

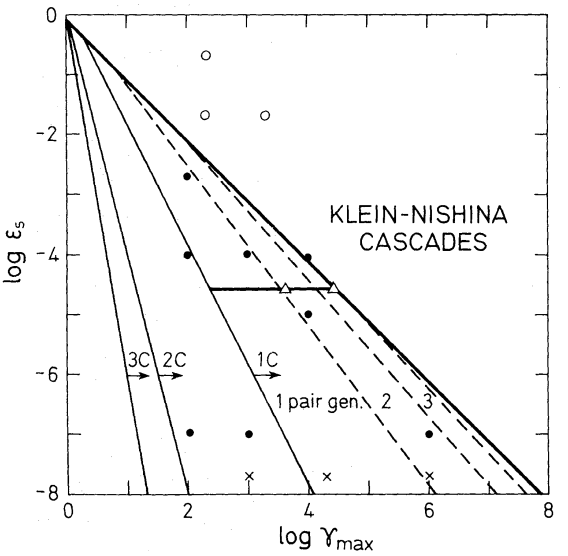

Figure 1. Parameter space (ε_s, γ_{max}) for non-thermal pair cascades, where ε_s is the photon energy of the soft mono-energetic radiation and γ_{max} is the maximum Lorentz factor of injected primary particles. Above the diagonal thick solid line most interactions take place in the Klein–Nishina limit, while below the line at least first-order Compton scatterings are in the Thomson limit. Three solid lines labelled 1C, 2C, 3C mark the boundaries of the regions, where photons at ε_s by scattering one, two or three times reach the pair production threshold. The parameter space covering first-order Compton cascades (1C) is further divided into regions characterized by the number of pair generations in the cascade. Parameters used in recent work are marked: △ ZL85, • F86, × Stern (1985), ○ Aharonian *et al.* (1985). The △-case on the solid diagonal line was also studied by F86 and Kardashev, Novikov & Stern (1986). Cases studied in this paper lie on the thick horizontal line.

Besides γ_{max} and ε_s there are two further parameters: the compactness parameters of the injected luminosities ℓ_i and ℓ_s. For $\ell_s \gg \ell_i$ the dependence on ℓ_s is negligible (ZL85 and below). For given γ_{max} and ε_s we will determine the properties of the pair cascade with increasing compactness ℓ_i.

2.2 THE INTEGRAL EQUATION

The spectral energy distribution of pairs, $N(\gamma)\,\mathrm{cm}^{-3}$, at Lorentz factor γ and of photons, $n(\gamma)\,\mathrm{cm}^{-3}$, at dimensionless photon energy ε (units of mc^2) are determined by the kinetic equations for respective species. Here the approach of ZL85 is adopted, where the integro-differential equations are converted into a simple integral equation.

Another approach is to solve the kinetic equations numerically (F86). We start the discussion with the kinetic equations, partly to show the near equivalence of the two approaches and partly to explain the physical effects included besides those of ZL85.

The two steady-state kinetic equations at relativistic energies γ, $\varepsilon > 1$ are

$$\dot{N}_C(\gamma) + P(\gamma) + Q(\gamma) = 0 \tag{2.9}$$

$$\dot{n}_C^{NT}(\varepsilon) + \dot{n}_C^{T}(\varepsilon) + \dot{n}_{\gamma\gamma}(\varepsilon) - c\,\frac{dn}{ds}(\varepsilon) = 0. \tag{2.10}$$

The terms in equation (2.9) represent the rate of change in the number density of particles at γ due to Compton scatterings, due to injection from photon–photon pair production and due to a source function $Q(\gamma)\,\mathrm{cm}^{-3}\,\mathrm{s}^{-1}$, respectively. The terms in equation (2.10) represent the injection of photons at energy ε due to non-thermal up-scattering by relativistic particles, thermal

down-scattering by a cooled non-relativistic particles, photon–photon absorption and a radiative transfer term (along the path-length ds), respectively.

When relativistic particles Thomson cool on soft photons with density $n_s\,\mathrm{cm}^{-3}$ at photon energy ε_s, then the first term in equation (2.9) becomes

$$\dot{N}_C(\gamma)=-\frac{\partial}{\partial\gamma}\dot{\gamma}_C N(\gamma)\quad \mathrm{cm}^{-3}\,\mathrm{s}^{-1} \tag{2.11}$$

with the cooling rate $\dot{\gamma}_C=-(4/3)\sigma_T c n_s\varepsilon_s\gamma^2$. Equation (2.9) is integrated to give the relativistic particle spectrum

$$N(\gamma)=(4/3\sigma_T c n_s\varepsilon_s\gamma^2)^{-1}\int_{\gamma}^{\gamma_{max}}[Q(\gamma')+P(\gamma')]\,d\gamma'\quad \mathrm{cm}^{-3}, \tag{2.12}$$

where γ_{max} is the maximum injected Lorentz factor. The relativistic particles up-scatter the soft photons at ε_s to the photon energy ε at the rate (using equation B2)

$$\dot{n}_C^{NT}(\varepsilon)=\frac{\varepsilon_s}{12}\left(\frac{3}{\varepsilon\varepsilon_s}\right)^{3/2}\int_{(3\varepsilon/4\varepsilon_s)^{1/2}}^{\gamma_{max}}[Q(\gamma')+P(\gamma')]\,d\gamma'\quad \mathrm{cm}^{-3}\,\mathrm{s}^{-1}\qquad (4/3\varepsilon_s<\varepsilon<\varepsilon_{max,1}). \tag{2.13}$$

As noted by ZL85, $\dot{n}_C^{NT}(\varepsilon)$ is *independent* of the soft photon density n_s. The suppressing effect on $N(\gamma)$ of larger n_s is cancelled by the enhanced scattering rate. As this is the only point where the soft photon density could enter in the cascade calculations in a major way, the cascade is (almost) independent of n_s (or L_s or ℓ_s).

Replacing the radiative transfer term in equation (2.10) by a mean escape probability and assuming that thermal down-scattering by cold pairs effectively removes the scattered photon from the range $\varepsilon>1$, then it is shown in Appendix A that the photon kinetic equation can be rewritten as

$$\dot{n}_{\gamma\gamma}(\varepsilon)=-\dot{n}_C^{NT}(\varepsilon)[1-\mathscr{E}(\varepsilon)]\mathscr{R}(\varepsilon), \tag{2.14}$$

where

$$\mathscr{E}(\varepsilon)=\frac{1-\exp[-\tau_{abs}(\varepsilon)]}{\tau_{abs}(\varepsilon)}, \tag{2.15}$$

$$\mathscr{R}(\varepsilon)=\tau_{\gamma\gamma}(\varepsilon)/\tau_{abs}(\varepsilon), \tag{2.16}$$

and

$$\tau_{abs}(\varepsilon)=\tau_{\gamma\gamma}(\varepsilon)+\tau_C(\varepsilon). \tag{2.17}$$

Here, $\tau_{\gamma\gamma}(\varepsilon)=a_{\gamma\gamma}(\varepsilon)R$ is the pair absorption optical depth with the absorption coefficient given in Appendix B2, while $\tau_C(\varepsilon)=[\sigma_C(\varepsilon)/\sigma_T]\tau_T$ is the exact Compton scattering optical depth in a cold plasma with the cross-section $\sigma_C(\varepsilon)$ given in, e.g. Jauch & Rohrlich (1976). Equation (2.14) is easily interpreted as follows: the rate of pair production at ε is equal to the photon injection rate times the photon fraction that suffers either photon–photon absorption or down-scattering, $1-\mathscr{E}(\varepsilon)$, times the fraction of 'absorptions' that give rise to pairs, $\mathscr{R}(\varepsilon)$.

Following ZL85 the pair (particle) injection term $P(\gamma)\,\mathrm{cm}^{-3}\,\mathrm{s}^{-1}$ in equation (2.9) is proportional to the photon–photon pair production term $\dot{n}_{\gamma\gamma}(\varepsilon)\,\mathrm{cm}^{-3}\,\mathrm{s}^{-1}$. As there are two particles produced per event with energy $\gamma=\varepsilon/2$ the two rates are related through

$$P(\gamma)=-4\dot{n}_{\gamma\gamma}(2\gamma)=4\dot{n}_C^{NT}(2\gamma)[1-\mathscr{E}(2\gamma)]\mathscr{R}(2\gamma). \tag{2.18}$$

The two important equations (2.13) and (2.18) relate the pair injection rate $P(\gamma)$ to the

non-thermal photon injection rate $\dot{n}_C^{NT}(\varepsilon)$. Either of them can be eliminated to give an integral equation for the other rate. Eliminating $P(\gamma)$ gives (*cf.* equation 8 in ZL85)

$$\dot{n}_C^{NT}(\varepsilon)=\frac{\varepsilon_s}{12}\left(\frac{3}{\varepsilon\varepsilon_s}\right)^{3/2}\int_{(3\varepsilon/4\varepsilon_s)^{1/2}}^{\gamma_{max}}\{Q(\gamma')+4\dot{n}_C^{NT}(2\gamma')[1-\mathscr{E}(2\gamma')]\mathscr{R}(2\gamma')\}\,d\gamma, \tag{2.19}$$

which is the final form of the integral equation for first-order Compton pair cascades in dominant soft photon backgrounds. Once $\dot{n}_C^{NT}(\varepsilon)$ has been solved for, $P(\gamma)$ is obtained from equation (2.18). Two further equations relating τ_T and $\tau_{\gamma\gamma}$ [appearing in $\mathscr{E}(2\gamma)$ and $\mathscr{R}(2\gamma)$] to $P(\gamma)$ or $\dot{n}_C^{NT}(\varepsilon)$ are needed.

The injected primary particles (which are taken to be pairs) and the secondary pairs injected during the cascade all Thomson cool on the soft photons at ε_s down to non-relativistic energies, where they thermalize through Coulomb collisions before annihilating (e.g. Crannell *et al.* 1976). The steady density (and Thomson depth) of cold pairs is determined by pair equilibrium. Balancing the annihilation rate, equation (C7), with the total pair injection rate, $\frac{1}{2}\int[Q(\gamma)+P(\gamma)]\,d\gamma$ gives (ZL85)

$$\tau_T=\left[g_a^{-1}\frac{16}{3}\frac{\sigma_T R^2}{c}\int_1^{\gamma_{max}}[Q(\gamma)+P(\gamma)]\,d\gamma\right]^{1/2}, \tag{2.20}$$

where g_a (given by equation C8) is a temperature-dependent correction factor to the Born annihilation rate. (The correction to τ_T is larger than a factor of 2 only for very small temperatures, $kT/mc^2<10^{-4}$).

The optical depth to photon–photon pair production is written using equation (B3) as

$$\tau_{\gamma\gamma}(\varepsilon)=\eta\sigma_T\frac{1}{\varepsilon}n\left(\frac{1}{\varepsilon}\right)R, \tag{2.21}$$

where η is taken to be 0.2 (Appendix B2). As equation (2.21) is to be used in equation (2.19) for $\varepsilon>1$, the photon spectral density at $\varepsilon<1$ needs to be known. When $\tau_T>1$ Compton scatterings on cold thermal pairs modify the shape of the injected photon spectrum above $\varepsilon_{break}\equiv 1/\tau_T^2$ (e.g. Sunyaev & Titarchuk 1980). Instead of solving the full radiative transfer problem at $\varepsilon<1$ [i.e. equation 2.10 but deleting the $\dot{n}_{\gamma\gamma}(\varepsilon)$-term] a simple analysis gives a prescription of the effects. Writing the spectral photon density at $\varepsilon<1$ as

$$n(\varepsilon)=\frac{R}{c}\dot{n}_C^{NT}(\varepsilon)\,\mathscr{E}(\varepsilon) \tag{2.22}$$

all the radiative transfer effects are contained in $\mathscr{E}(\varepsilon)$ (*cf.* equation A5 for $\varepsilon>1$). As the cascade is considered at some average *internal* point in the pair cloud the radiative transfer factor to be used is

$$\mathscr{E}(\varepsilon)=\left(1+\frac{\tau_T}{3}\right)[1-\exp(-3/\varepsilon\tau_T^2)]\qquad(\varepsilon<1), \tag{2.23}$$

where the first factor approximately describes the diffusive enhancement of the photon density below ε_{break} and the second factor approximately describes a steepening beyond ε_{break}. The spectral index of the *internal* radiation field changes by unity across ε_{break} as is easily shown using the Kompaneets equation (keeping the recoil term only, see, e.g. Sunyaev & Titarchuk 1980) together with an escape and a power-law injection term. Below ε_{break} scattering is coherent and escape balances injection leading to the diffusive enhancement factor. The photons emitted in the interior above ε_{break} do not 'see' the surface before they reach ε_{break}. Therefore, above ε_{break} the

spectrum is determined by balancing the Kompaneets down-scatter term with the injection term. The *internal* steepening by unity at $\varepsilon_{\rm break}$ is independent of the details of the escape and thus of the actual spatial distribution of scatterers. In the radiation field given by equation (2.22) the pair absorption optical depth becomes

$$\tau_{\gamma\gamma}(\varepsilon)=\eta\,\frac{\sigma_{\rm T}R^2}{c}\,\frac{1}{\varepsilon}\,\dot{n}_{\rm C}^{\rm NT}\!\left(\frac{1}{\varepsilon}\right)\mathscr{E}\!\left(\frac{1}{\varepsilon}\right). \tag{2.24}$$

The three equations (2.19), (2.20) and (2.24) can now be solved numerically for $\dot{n}_{\rm C}^{\rm NT}(\varepsilon)$ given R, $\varepsilon_{\rm s}$, and $Q(\gamma)$. However, when the optical depths are much larger than unity, then equation (2.19) becomes independent of both $\tau_{\gamma\gamma}(\varepsilon)$ and $\tau_{\rm C}(\varepsilon)$, and equations (2.20) and (2.24) are no longer needed. This is the case of saturated pair production and it is solved analytically in Section 3.

2.3 THE PAIR YIELD

A convenient derived parameter describing the efficiency in creating pairs is the pair yield, x, i.e. the fraction of injected power that is converted into pair rest mass. The pair yield is obtained using

$$x=\frac{\displaystyle\int_1^{\gamma_{\max,1}} P(\gamma)\,d\gamma}{\displaystyle\int_1^{\gamma_{\max}} Q(\gamma)(\gamma-1)\,d\gamma}. \tag{2.25}$$

Energy conservation requires that $x\leq 1$ (provided pair annihilation photons do not produce further pairs). As the compactness parameter of the primary particle power is

$$\ell_{\rm i}=\frac{L_{\rm i}}{R}\,\frac{\sigma_{\rm T}}{mc^3}=\frac{4\pi}{3}\,\frac{\sigma_{\rm T}R^2}{c}\int_1^{\gamma_{\max}} Q(\gamma)(\gamma-1)\,d\gamma \tag{2.26}$$

it is clear from equations (2.20) and (2.25) that the pair yield is related to the Thomson depth of secondary pairs through (Guilbert *et al.* 1983)

$$x=g_{\rm a}\,\frac{\pi}{4}\,\frac{\tau_{\rm T,sec}^2}{\ell_{\rm i}}. \tag{2.27}$$

3 Saturated pair production

The pair production at photon energy ε is saturated when, by far, most photons at ε produce pairs rather than escape or down-scatter. Then the integral equation (2.19) for the cascade has an analytical solution.

3.1 THE GENERAL SOLUTION

Saturation at ε requires that $\tau_{\gamma\gamma}(\varepsilon)\gg 1$ and that $\tau_{\gamma\gamma}(\varepsilon)\gg\tau_{\rm C}(\varepsilon)$ or, equivalently, that $\mathscr{E}(\varepsilon)=0$ and $\mathscr{R}(\varepsilon)=1$. In the range of photon energies where these conditions hold the integral equation (2.19) becomes

$$\dot{n}_{\rm C}^{\rm NT}(\varepsilon)=\frac{\varepsilon_{\rm s}}{12}\left(\frac{3}{\varepsilon\varepsilon_{\rm s}}\right)^{3/2}\int_{(3\varepsilon/4\varepsilon_{\rm s})^{1/2}}^{\gamma_{\max}}[Q(\gamma')+4\dot{n}_{\rm C}^{\rm NT}(2\gamma')]\,d\gamma', \tag{3.1}$$

while

$$P(\gamma)=4\dot{n}_{\mathrm{C}}^{\mathrm{NT}}(2\gamma). \tag{3.2}$$

Physical (rather than mathematical) insight allows the general solution of equation (3.1) to be written down directly. Assume that besides the injected primary particles there are K pair generations and consequently $K+1$ photon generations in the cascade. Denote the kth generation by $\dot{n}_k(\varepsilon)$. Then

$$\dot{n}_{\mathrm{C}}^{\mathrm{NT}}(\varepsilon)=\sum_{k=1}^{K+1}\dot{n}_k(\varepsilon). \tag{3.3}$$

Define the kth cascade function as

$$S_k(z)=4\frac{\dot{n}_k(\varepsilon)}{\dot{N}} \tag{3.4}$$

with

$$z=\tfrac{1}{3}\varepsilon\varepsilon_{\mathrm{s}} \tag{3.5}$$

and $\dot{N}\,\mathrm{cm}^{-3}\,\mathrm{s}^{-1}$ being a constant, to appear in the injection rate $Q(\gamma)$. The integral equation becomes

$$\sum_{k=1}^{K+1}S_k(z)=\tfrac{1}{2}z^{-3/2}\int_{z^{1/2}}^{z_{\mathrm{T}}}\left[\frac{Q(3z'/2\varepsilon_{\mathrm{s}})}{\dot{N}}+\sum_{k=1}^{K}S_k(z')\right]dz', \tag{3.6}$$

where

$$z_{\mathrm{T}}=\tfrac{2}{3}\gamma_{\max}\varepsilon_{\mathrm{s}}<\tfrac{1}{2} \tag{3.7}$$

(i.e. the Thomson limit) is an important parameter. As the last term in the integrand in equation (3.1) really is $P(\gamma')$ (*cf.* equation 2.13) only K terms in the sum over S_k have been included. The left-hand side of equation (3.6) is essentially the up-scattered spectrum produced by the injected particles appearing in the integrand on the right-hand side. The primary injection $Q(\gamma)$ gives rise to the first photon generation and the kth pair generation gives rise to the $(k+1)$th photon generation. Thus, one can identify the $K+1$ terms on the left-hand side with the $K+1$ terms on the right-hand side of equation (3.6), giving

$$S_1(z)=\tfrac{1}{2}z^{-3/2}\int_{z^{1/2}}^{z_{\mathrm{T}}}\frac{Q(3z'/2\varepsilon_{\mathrm{s}})}{\dot{N}}dz' \tag{3.8}$$

and

$$S_{k+1}(z)=\tfrac{1}{2}z^{-3/2}\int_{z^{1/2}}^{z_{\mathrm{T}}^{k}}S_k(z')\,dz' \tag{3.9}$$

for $k=1.\ldots,K$ and properly accounting for the maximum Lorentz factor of the kth pair generation.

It is convenient to discuss the cascades in terms of the injected power per unit logarithmic energy interval. Define the new cascade functions $T_k(y)$ as

$$T_k(y_k)=\frac{\varepsilon^2}{4\gamma_{\max}}S_k(z)=\frac{\varepsilon^2}{\gamma_{\max}}\frac{\dot{n}_k(\varepsilon)}{\dot{N}} \tag{3.10}$$

with

$$y_k=\frac{z}{z_T^{2^k}}=\frac{\varepsilon}{\varepsilon_{\max,k}} \qquad (y_k\leq 1) \tag{3.11}$$

being a function of z, z_T, *and* k. The solutions, equations (3.8) and (3.9), become

$$T_1(y_1)=\tfrac{1}{2}y_1^{1/2}\int_{y_1^{1/2}}^{1}\frac{Q(\gamma_{\max}y_0)}{\dot{N}}\gamma_{\max}\,dy_0 \tag{3.12}$$

and

$$T_{k+1}(y_{k+1})=\tfrac{1}{2}y_{k+1}^{1/2}\int_{y_{k+1}^{1/2}}^{1}y_k^{-2}T_k(y_k)\,dy_k. \tag{3.13}$$

The full cascade for a given z_T is given by the sum of the cascade functions

$$T(z)=\sum_{k=1}^{K}T_k(y_k). \tag{3.14}$$

The cascade functions $T_k(y_k)$ can now be explicitly calculated for a given injection spectrum $Q(\gamma)$ using equations (3.12) and (3.13). The particle and photon injection rates are then determined from equations (3.2) and (3.10) (or equations D1 and D2).

3.2 MONO-ENERGETIC PARTICLE INJECTION

The cascade functions $T_k(y)$ for mono-energetic injection

$$Q(\gamma)=\dot{N}\delta(\gamma-\gamma_{\max}) \tag{3.15}$$

where $\dot{N}\,\mathrm{cm}^{-3}\,\mathrm{s}^{-1}$ is the particle injection rate, are given in Appendix D1. Fig. 2 shows $T_k(y)$ as a function of y for the first four generations. Two examples of actual cascades are shown in Fig 3(a) and (b) for $z_T=0.05$ and 0.5, respectively. For a given soft photon energy ε_s, the validity of the saturated cascade functions extend down to $z=z_m$, when representing the pair generations and down to z_m^2 when representing photon generations. Here

$$z_m=\tfrac{1}{3}\varepsilon_{\min}\varepsilon_s \tag{3.16}$$

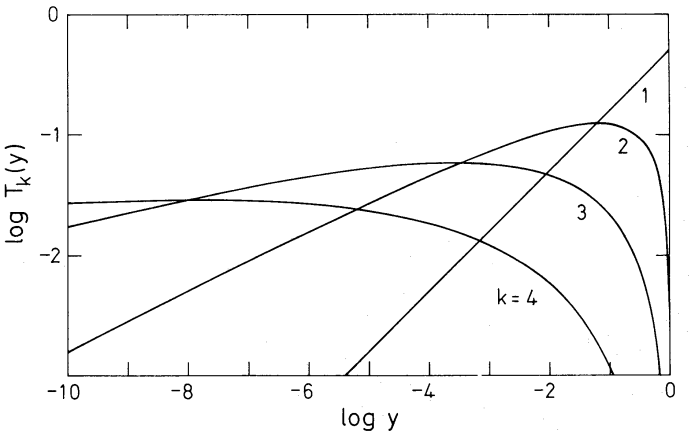

Figure 2. The saturated cascade functions $T_k(y)$ for each generation k as a function of y for the case of steady mono-energetic particle injection. See text and Appendix D.

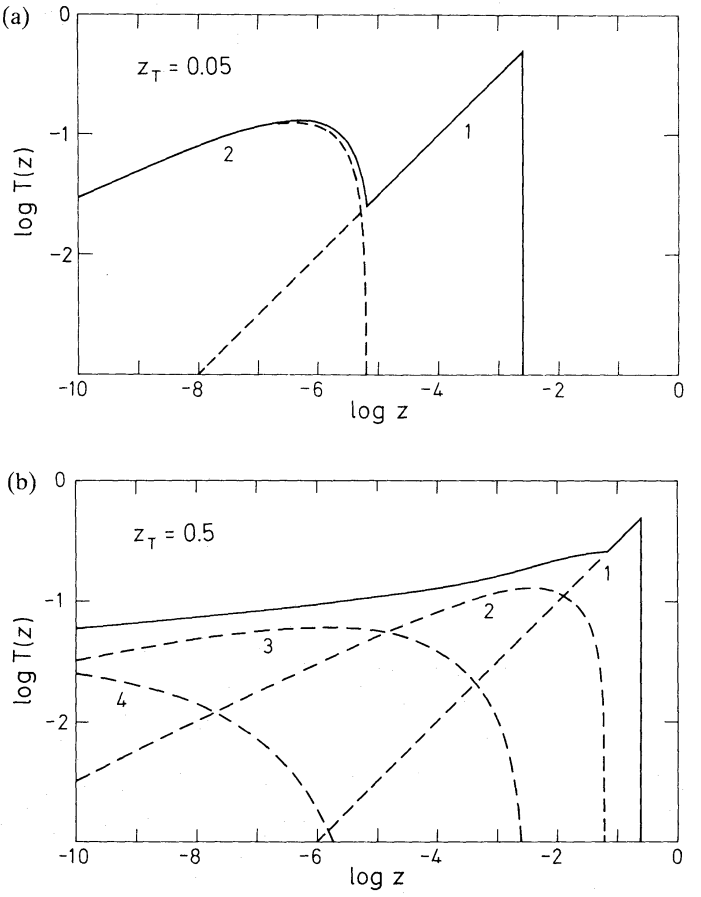

Figure 3. (a) The cascade function $T(z)$ (solid curve) for saturated pair cascades initiated by steady injection of mono-energetic particles. $T(z)$ is proportional to the injected secondary power per logarithmic energy interval. The 1st and 2nd generations (dashed curves) are well separated for $z_T=0.05$. Characteristic spectral indices are $\alpha_1=0.5$ and $\alpha_2=0.75$ for respective generation. See text and Appendix D for details and definitions. (b) Same as (a) but for $z_T=0.5$. Four generations (dashed curves) overlap giving a spectral index $\alpha\approx0.92-0.95$.

with $\varepsilon_{\min}$ defining the minimum effective photon energy for which saturated pair production takes place. From Figs 2 and 3 it is seen that:

(i) The shapes of the generations are independent of z_T. They are shifted apart at small z_T but overlap more and more as z_T approaches unity (as the upper cut-offs are equal to $z_T^{2^k}$).

(ii) Each generation has a power law behaviour at small energies and an upper cut-off that becomes increasingly smoother and broader with increasing k.

(iii) The injected photon spectrum is no longer given by that from the primary particles (with spectral index $\alpha=\frac{1}{2}$) but is dominated by discrete generations for $z_T\ll1$ (giving a strongly energy dependent α in Fig. 3a) and is dominated by the sum of overlapping generations for $z_T\lesssim1$ (giving $\alpha\approx0.95$ over many decades in Fig. 3b).

The change in α of the power law part of each photon generation from $\alpha=\frac{1}{2}$ towards $\alpha=1$ as evident in Fig. 2 comes about as follows. The injected primary particles Thomson cool giving $N(\gamma)\propto\gamma^{-m_0}$ with $m_0=2$ while producing the first photon generation with $\alpha_1=(m_0-1)/2=\frac{1}{2}$. Saturation means that all photons produce pairs making the pair injection $P(\gamma)\propto\gamma^{-p_1}$ to have $p_1=\alpha_1+1=\frac{3}{2}$. Thomson cooling causes the first pair generation to have $N(\gamma)\propto\gamma^{-m_1}$ with $m_1=p_1+1=\frac{5}{2}$. Then the intensity index of the second photon generation becomes

$\alpha_2=(m_1-1)/2=0.75$. Continuing the argument gives for the kth generation

$$p_k=2-2^{-k}, \tag{3.17a}$$

$$m_k=p_k+1=3-2^{-k}, \tag{3.17b}$$

$$\alpha_k=\tfrac{1}{2}(m_{k-1}-1)=1-2^{-k}, \tag{3.17c}$$

or, recursively,

$$p_{k+1}=(p_k+2)/2,$$

$$m_{k+1}=(m_k+3)/2,$$

$$\alpha_{k+1}=(\alpha_k+1)/2,$$

with

$$\alpha_3=0.875$$

and

$$\alpha_4=0.9375.$$

For large k, the steady particle distribution approaches $N(\gamma)\propto\gamma^{-3}$ while the intensity index of the photons becomes $\alpha=1$. Thomson cascades have at most about three generations (see Fig. 1) and these limiting indices are never approached.

For small z_T each photon generation dominates the injection spectrum over a large energy interval (Fig. 3a). For appropriate choices of z_T and ε_s (or γ_{max} and ε_s) the power law part of the second photon generation dominates in the X-ray range giving $\alpha\approx0.8$, slightly larger than the asymptotic value ¾ which is approached only at very small photon energies.

For z_T closer to unity the separate spectral shapes of each generation cannot be distinguished in the total injection spectrum. In the range $10^{-10}<z<10^{-4}$ in Fig. 3(b), where generations 2 and 3 (with $\alpha=0.75$ and 0.875, respectively) dominate, the overall spectral index α varies slowly between 0.95 and 0.92, i.e. almost constant injected power per logarithmic energy interval. This is simply due to energy conservation as most of the injected photon power of each generation (except the fraction below threshold $\varepsilon=2$) gets reprocessed into the next generation.

The saturated pair yield of the kth pair generation when mono-energetic injection takes place is given by (using equations 2.25, 3.2, and 3.10)

$$x_k=\left(\frac{2}{\varepsilon_{\min}}\right)w_{k+1}^{1/2}\int_{w_{k+1}^{1/2}}y_k^{-2}T_k(y_k)\,dy_k, \tag{3.18}$$

where

$$w_{k+1}=\left(\frac{z_m}{z_T^{2^k}}\right)^2=\left(\frac{\varepsilon_{\min}}{\varepsilon_{\max,k}}\right). \tag{3.19}$$

Using the solution to the integral equation, equation (3.13), the pair yield of the kth generation is simply related to the cascade function of the next generation,

$$x_k=\left(\frac{2}{\varepsilon_{\min}}\right)2T_{k+1}(w_{k+1}). \tag{3.20}$$

Fig. 4 shows the pair yield from the first pair generation (dotted curves) as a function of the maximum energy $\varepsilon_{max,1}$ of the first photon generation. The pair yield for the first pair generation

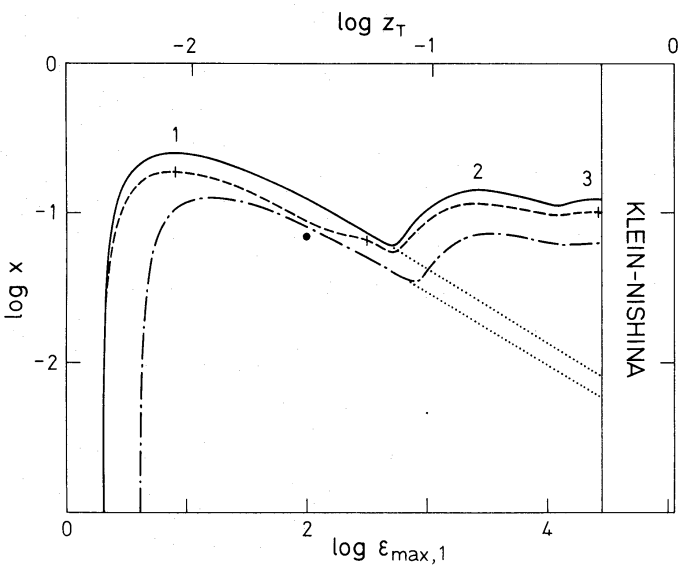

Figure 4. The saturated pair yield, x, (obtained from the analytical cascade functions) as a function of the maximum photon energy $\varepsilon_{max,1}$ or of z_T for the case of mono-energetic particle injection and $\varepsilon_s=2.7\times10^{-5}$. The solid curve show the sum of the pair yields from different generations for the minimum effective pair-producing photon energy $\varepsilon_{min}=2$. The dashed–dotted curve is the total pair yield for $\varepsilon_{min}=4$. The pair yield from the first generation (dotted curves) is independent of the choice of ε_s. The dashed curve shows the saturated pair yields obtained by numerically solving equation (4.2) for $\ell_i=4\times10^3$ including the effects of down-scattering. Vertical bars show the location of the solutions displayed in Figs 6–11. The dot shows the saturated pair yield obtained by F86 for $\ell_i=4.2\times10^3$.

can be written as

$$x_1=\left(\frac{1-\alpha_1}{\alpha_1}\right)\frac{2}{\varepsilon_{max,1}}\left[\left(\frac{\varepsilon_{max,1}}{\varepsilon_{min}}\right)^{\alpha_1}-1\right] \qquad (\alpha_1<1) \tag{3.21}$$

depending only on $\varepsilon_{max,1}$, the minimum effectively pair producing photon energy ε_{min}, and the spectral index, α_1, of the pair-producing photons (here, $\alpha_1=\frac{1}{2}$). x_1 is zero for $\varepsilon_{max,1}<\varepsilon_{min}$ and has a maximum value of $2(1-\alpha_1)^{1/\alpha_1}\varepsilon_{min}^{-1}=\frac{1}{2}\varepsilon_{min}^{-1}$ at $\varepsilon_{max,1}=(1-\alpha_1)^{-1/\alpha_1}\varepsilon_{min}=4\varepsilon_{min}$. For $\varepsilon_{min}=2$, the maximum value, $x_1=25$ per cent, occurs at $\varepsilon_{max,1}=8$. The pair yields for the later pair generations depend on one further parameter (either γ_{max} or ε_s) taken to be $\varepsilon_s=2.7\times10^{-5}$ in Fig. 4. The solid and dashed–dotted curves show the total pair yield when $\varepsilon_{min}=2$ and 4, respectively. Nothing in our treatment excludes ε_{min} from taking values between 1 and 2 (formally giving pairs with Lorentz factors between $\frac{1}{2}$ and 1). However, as will be seen in Section 4.1, down-scatter dominates over pair absorption below $\varepsilon\approx2$–3, making $\varepsilon_{min}\approx2$–3. Irrespective of the details it is clearly seen in Fig. 4 that the saturated pair yield (once $\varepsilon_{max,1}>$a few$\times\varepsilon_{min}$) fluctuates in the narrow range of 0.06 to 0.25, while $\varepsilon_{max,1}$ changes by many order of magnitudes.

3.3 POWER LAW PARTICLE INJECTION

The cascade functions for power law injection

$$Q(\gamma)\,d\gamma=\dot{N}\left[\frac{\gamma}{\gamma_{max}}\right]^{-\Gamma}\frac{d\gamma}{\gamma_{max}} \qquad (1<\gamma<\gamma_{max}) \tag{3.22}$$

are given in Appendix D2. The constant, $\dot{N}\,\mathrm{cm}^{-3}\,\mathrm{s}^{-1}$, is equal to $(1-\Gamma)$ times the particle injection rate when $\Gamma<1$ and $\gamma_{max}\gg1$. Fig. 5(a) and (b) show $T(z)$ for $z_T=0.5$ and for $\Gamma=1.2$ and 2, respectively.

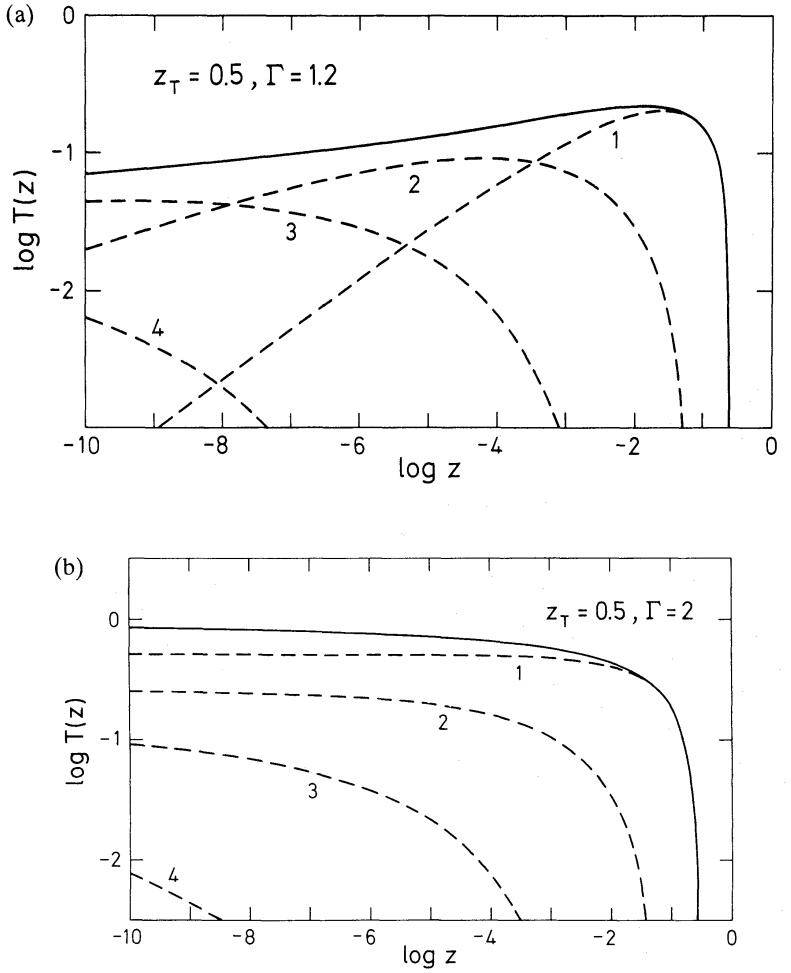

Figure 5. (a) The total cascade function $T(z)$ (solid curve) for saturated pair cascades initiated by power law injection of particles with number index $\Gamma=1.2$. $T(z)$ is proportional to the injected power per logarithmic energy interval. The parameter $z_T=0.5$ is large and the four generations (dashed cuves) overlap giving a spectral index $\alpha\approx0.92$–0.95 for the sum of the generations. The shape of the solid curve below $z=10^{-4}$ is indistinguishable from that in Fig. 3(b). See text and Appendix D for details and definitions. (b) Same as (a) but for $\Gamma=2$, i.e. equal primary power is injected per logarithmic energy interval and reprocessing is ineffective.

For $\Gamma<2$ most of the injected power is at $\gamma_{\max}$ and the pair cascade can reprocess the power towards lower energies just as for mono-energetic injection. Similar arguments as these in Section 3.2 give the indices for the low-energy part of the kth generation as

$$p_k=2-(2-\Gamma)2^{-k} \tag{3.23a}$$

$$m_k=3-(2-\Gamma)2^{-k} \tag{3.23b}$$

$$\alpha_k=1-(2-\Gamma)2^{-k} \tag{3.23c}$$

when $\Gamma>1$, while the indices are the same as those for mono-energetic injection, equations (3.17), when $\Gamma<1$. The recursive relations are always the same. The case $\Gamma=1.2$ gives $\alpha_1=0.6$, $\alpha_2=0.8$ and $\alpha_3=0.9$, while the total injection spectrum has an intensity index that is almost constant ($\alpha\propto0.92$–0.95) over the range $10^{-10}<z<10^{-4}$ as seen in Fig. 5(a). Comparing the total injection spectra in Figs 3(b) and 5(a) shows that the shapes are remarkably similar. Aligning the two spectra at, e.g. $z=10^{-9}$ gives deviations over the range $10^{-10}<z<10^{-3}$ by at most ±1.5 per cent, although the individual generations in each case are quite different. At this point it is

appropriate to comment upon the solution to the saturated integral equation for mono-energetic injection given by ZL85 (their equation 15). ZL85 set the upper integration limit in equation (3.1) equal to infinity and then solve the equation getting an infinite sum with the first few terms being equal to the first term of the first few cascade functions given in Appendix D1. The large number of terms (beyond the first few) nearly proportional to z^{-2} adds a finite but large contribution making $T(z)$ to be about a factor 10 larger than the exact result in Fig. 3(b). The *shape*, however, is again remarkably similar to that of Figs 3(b) and 5(a). Aligning with the spectrum in Fig. 3(b) gives deviations by no more than ±1 per cent. The influence of the initial conditions [i.e. $Q(\gamma)$] at large z obviously decreases as the integral equation processes this information towards smaller z, and a unique spectral shape results with a slowly varying (but *not* constant) spectral index. This unique shape occurs only when there are many overlapping generations, i.e. z_T cannot be much smaller than unity.

Kazanas (1984) treated the case of power law particle injection showing the resulting $N(\gamma)$ for $\Gamma=1.2$ (*cf.* Fig. 5a). In solving the integral equation he put the upper integration limit equal to infinity obtaining an infinite sum similar to that of ZL85. In making such an approximation all the physical details of the different cascade generations, so beautifully hidden within the integral equation, are irrevocably lost.

When $\Gamma=2$ (Fig. 5b) then equal particle power is injected per logarithmic energy interval and redistribution towards smaller energies has little effect. Each injected generation has $\alpha=1$ at small energies and a decreasing amplitude due to leakage of radiation below threshold. The first photon generation dominates at all energies for $\Gamma=2$ and becomes increasingly dominant for larger Γ with the spectral index being $\alpha=\alpha_1=\Gamma/2$. The pair cascade has a negligible effect as shown by the figures in Zdziarski (1986) for Γ in the range 2.4 to 2.6.

4 Unsaturated pair production for mono-energetic particle injection

The pair production at photon energy ε is unsaturated when some photons at ε escape rather than produce pairs.

It is of conceptual advantage to first discuss the *injected* pair and photon spectra (Section 4.1) and then to apply modifying radiative transfer factors to the injected spectrum to obtain the *emerging* photon spectrum (Section 4.3).

4.1 INJECTED PAIR AND PHOTON SPECTRA

The relationship between the injected compactness ℓ_i and the primary pair injection rate, $\dot{N}\,\mathrm{cm^{-3}\,s^{-1}}$, is simple for mono-energetic particle injection. From equations (2.26) and (3.15),

$$\ell_i=\frac{4\pi}{3}\frac{\sigma_T R^2}{c}\dot{N}\gamma_{max}\qquad(\gamma_{max}\gg 1). \tag{4.1}$$

Similarly, the three equations (2.19), (2.20), and (2.24) simplify into

$$\frac{\dot{n}_C^{NT}(\varepsilon)}{\dot{N}}=\frac{\varepsilon_s}{12}\left(\frac{3}{\varepsilon\varepsilon_s}\right)^{3/2}\left\{1+4\int_{(3\varepsilon/4\varepsilon_s)^{1/2}}^{\gamma_{max,1}}\frac{\dot{n}_C^{NT}(2\gamma')}{\dot{N}}[1-\mathscr{E}(2\gamma')]\mathscr{R}(2\gamma')\,d\gamma'\right\} \tag{4.2a}$$

$$\tau_T=\left\{g_a^{-1}\frac{4}{\pi}\frac{\ell_i}{\gamma_{max}}\left[1+\int_1^{\gamma_{max,1}}\frac{P(\gamma)}{\dot{N}}d\gamma\right]\right\}^{1/2} \tag{4.2b}$$

$$\tau_{\gamma\gamma}(\varepsilon)=\eta\frac{3}{4\pi}\frac{\ell_i}{\gamma_{max}}\frac{1}{\varepsilon}\frac{\dot{n}_C^{NT}(1/\varepsilon)}{\dot{N}}\mathscr{E}\left(\frac{1}{\varepsilon}\right) \tag{4.2c}$$

where $\mathscr{R}(\varepsilon)$ is given by equation (2.16) and $\mathscr{E}(\varepsilon)$ by equation (2.15) for $\varepsilon>1$ and by equation (2.23) for $\varepsilon<1$. There are only three parameters in equations (4.2): ℓ_i, γ_{max}, and ε_s. The parameter space (γ_{max}, ε_s) can be divided into regions where different physical effects dominate. Within each region an increasing injection compactness ℓ_i will bring the dominant physical effect into action. The solutions of equations (4.2) will be discussed in three different regions in (γ_{max}, ε_s)-space using analytical methods and approximations whenever possible.

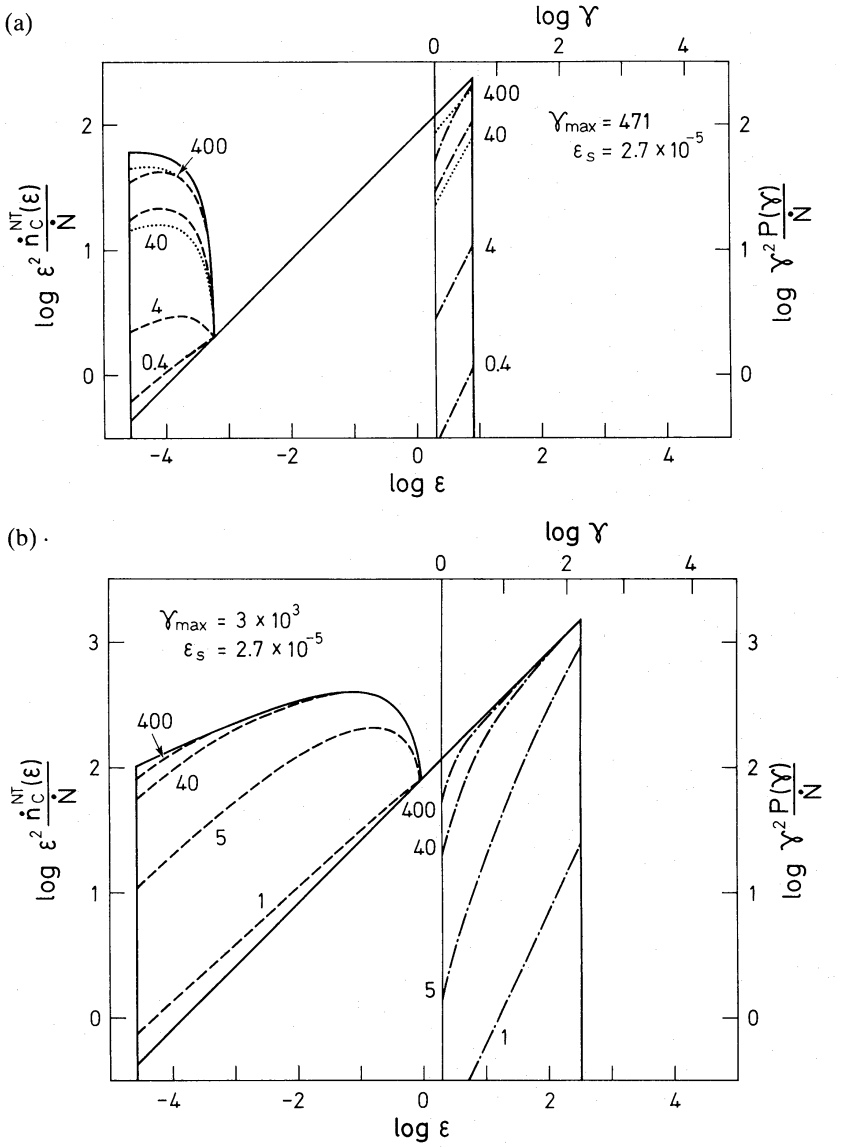

Figure 6. (a) The injected photon spectra [$\dot{n}_C^{NT}(\varepsilon)\,cm^{-3}s^{-1}$; dashed curves] and pair spectra [$P(\gamma)\,cm^{-3}s^{-1}$; dashed–dotted curves] in terms of the mono-energetic injection rate N. The spectra were obtained by solving equations (4.2) and they are shown as dimensionless injected power per logarithimc energy interval as functions of photon energy and Lorentz factor γ. Primary particles are injected at $\gamma_{max}=471$ with an injection compactness ℓ_i and soft photons at $\varepsilon_s=2.7\times10^{-5}$ (with $\ell_s=4\times10^3$ when determining the pair temperature). The solid curves show the two analytical cases of saturated pair production (neglecting down-scatter; see Section 3.2) and of negligible pair production ($\ell_i\ll1$; *cf.* equation 4.4). The approximate analytical solutions, equations (4.11) and (4.12), are shown by the dotted curves. The spectra are labelled by their values of ℓ_i. (b) Same as (a) but for $\gamma_{max}=3\times10^3$. Here $z_T\sim0.054$ (*cf.* Fig. 3a). Reprocessing through pair cascades becomes increasingly important as ℓ_i increases and the spectra approach the saturated analytical solution (the upper solid curve, *cf.* Fig. 3a) everywhere except near $\gamma=1$ and $\varepsilon=\varepsilon_s$ due to down-scatter. (c) Same as (a) but for $\gamma_{max}=2.7\times10^4$, which makes $z_T\approx0.5$ (*cf.* Fig. 3b). At $\ell_i=6$ there are three solutions of which the two stable to constant ℓ_i-perturbations are shown.

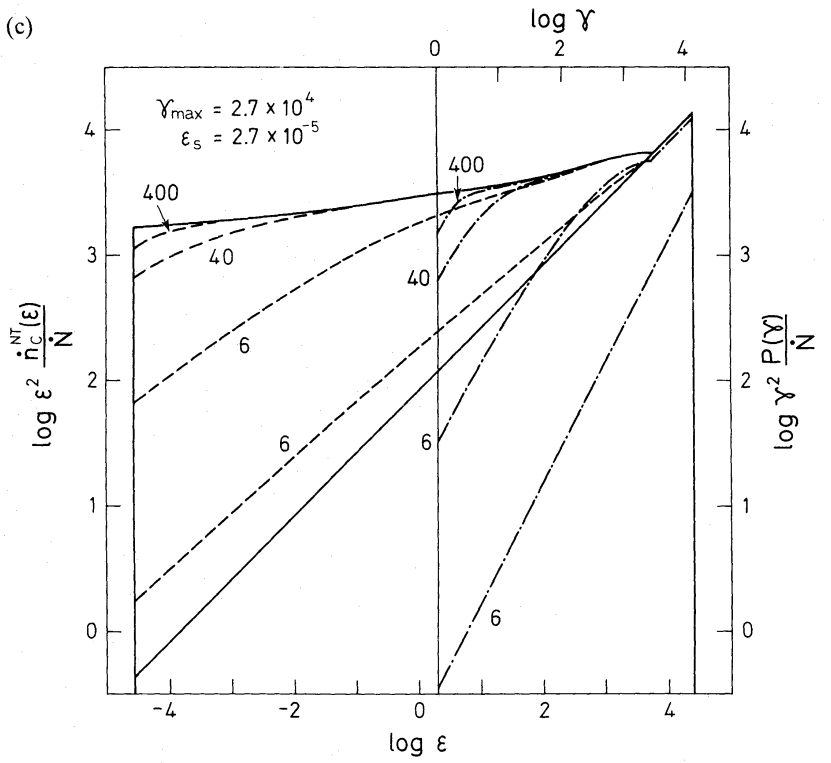

Figure 6–*continued*

Equation (4.2a) is also solved numerically in an iterative fashion by first setting $\dot{n}_C^{NT}(\varepsilon)=0$ in the integral and then feeding each iteration back into the integral. The number of iteration steps needed may be large, especially at the point where runaway pair production occurs (see below). However, when the pair production is saturated, then the iterative procedure exactly follows the analytical procedure in Section 3 (i.e. one further generation is added in each step) and the number of iterative steps needed is equal to the number of generations (plus one or two more if high numerical accuracy is wanted). The numerical solutions for three choices of γ_{max} are shown in Fig. 6(a)–(c) as the injected power per logarithmic energy interval. Each spectrum is labelled by its value of ℓ_i. All solutions are made for $\varepsilon_s=2.7\times10^{-5}$ corresponding to a blackbody temperature of 10^5 K typical of thermalized accretion discs around massive black holes. This choice as well as the chosen values of γ_{max} allow easy comparison with ZL85.

4.1.1 One secondary pair generation and no opacity feedback

For secondary pairs to be important at all (i.e. $\varepsilon_{max,1}>2$) and for pair-scattered (second-generation) photons not to cause any pair-producing opacity at $\varepsilon_{max,1}$ [i.e. $\varepsilon_{max,2}<(\varepsilon_{max,1})^{-1}$] requires

$$(\tfrac{2}{3}\varepsilon_s)^{-1/2}<\gamma_{max}<2^{-1/3}(\tfrac{2}{3}\varepsilon_s)^{-2/3} \tag{4.3}$$

or $2.4\times10^2<\gamma_{max}<1.2\times10^3$ for $\varepsilon_s=2.7\times10^{-5}$.

Fig. 6(a) shows the numerical solutions (dashed and dashed–dotted curves) as well as the analytical solutions (dotted curves, see below) wherever they deviate from the numerical ones. In Fig. 6(a) γ_{max} is equal to 471 making $\varepsilon_{max,1}=8$, i.e. the value of $\varepsilon_{max,1}$ at which the saturated pair yield peaks (see Fig. 4).

At $\varepsilon > \varepsilon_{\max,2}$, the total photon injection is just the photons scattered by the primary particles,

$$\frac{\dot{n}_C^{NT}(\varepsilon)}{\dot{N}} = \frac{\dot{n}_1(\varepsilon)}{\dot{N}} = \frac{\varepsilon_s}{12}\left(\frac{3}{\varepsilon\varepsilon_s}\right)^{3/2} \qquad (\varepsilon_{\max,2} < \varepsilon < \varepsilon_{\max,1}), \tag{4.4}$$

with most of the power being injected near $\varepsilon_{\max,1}$. Neglecting down-scatter and diffusion [i.e. setting $\mathscr{E}(1/\varepsilon)=1$ in equation (4.2c)] the pair absorption depth in the power law radiation field is obtained from equations (4.2c) and (4.4) as

$$\tau_{\gamma\gamma}(\varepsilon) = \frac{\ell_i}{\ell_c}\left(\frac{\varepsilon}{\varepsilon_{\max,1}}\right)^{1/2}, \tag{4.5}$$

which is less than unity for all $\varepsilon \le \varepsilon_{\max,1}$ as long as

$$\ell_i < \ell_c \equiv \eta^{-1}\frac{8\pi}{3} \approx 42\left(\frac{\eta}{0.2}\right)^{-1}. \tag{4.6}$$

A fraction $1-\mathscr{E}(\varepsilon)$ of the photons at ε pair produces giving the first and only secondary pair generation with the injection rate (using equations 2.18 and 4.4)

$$\frac{P_1(\gamma)}{\dot{N}} = \frac{\varepsilon_s}{3}\left(\frac{3}{2\gamma\varepsilon_s}\right)^{3/2}[1-\mathscr{E}(2\gamma)], \tag{4.7}$$

which is easily evaluated for any γ using equations (2.15) and (4.5). For small injection compactnesses, only a fraction $\tau_{\gamma\gamma}(\varepsilon)/2$ of the photons pair produces and equation (4.7) becomes (*cf.* equations 11–13 in ZL85)

$$\frac{P_1(\gamma)}{\dot{N}} = \frac{\varepsilon_s}{3}\left(\frac{3}{2\gamma\varepsilon_s}\right)^{3/2} \tfrac{1}{2}\tau_{\gamma\gamma}(2\gamma) = \frac{1}{4z_T}\left(\frac{\ell_i}{\ell_c}\right)\frac{1}{\gamma} \qquad (\ell_i \ll \ell_c), \tag{4.8}$$

while for $\ell_i \gg \ell_c$ all photons at ε pair produce and $P(\gamma)$ approaches the saturated solution [equations D1 and D6a or simply by setting $\mathscr{E}(2\gamma)=0$ in equation 4.7].

The pairs scatter the soft photons at ε_s to produce the second photon generation

$$\dot{n}_2(\varepsilon) = \frac{\varepsilon_s}{12}\left(\frac{3}{\varepsilon\varepsilon_s}\right)^{3/2}\int_{(3\varepsilon/4\varepsilon_s)^{1/2}}^{\gamma_{\max,1}} P_1(\gamma)\,d\gamma, \tag{4.9}$$

with $P_1(\gamma)$ given by equation (4.7). Making the approximation

$$1-\mathscr{E}(2\gamma) \approx \frac{\tfrac{1}{2}\tau_{\gamma\gamma}(2\gamma)}{1+\tfrac{1}{2}\tau_{\gamma\gamma}(2\gamma)} \tag{4.10}$$

gives an error less than 13 per cent as compared with equation (2.15) and makes the integral analytically tractable. Then the pair injection becomes

$$\frac{P_1(\gamma)}{\dot{N}} = \frac{1}{4z_T\gamma}\left(\frac{\ell_i}{\ell_c}\right)\frac{1}{1+(\ell_i/2\ell_c)(\gamma/\gamma_{\max,1})^{1/2}}, \tag{4.11}$$

while the photon injection caused by the pairs becomes

$$\frac{\dot{n}_2(\varepsilon)}{\dot{N}} = \frac{\varepsilon_s}{12}\left(\frac{3}{\varepsilon\varepsilon_s}\right)^{3/2}\frac{1}{2z_T}\left(\frac{\ell_i}{\ell_c}\right)\ln\left[\frac{(\varepsilon_{\max,2}/\varepsilon)^{1/4}+\ell_i/2\ell_c}{1+\ell_i/2\ell_c}\right] \qquad (\tfrac{4}{3}\varepsilon_s < \varepsilon < \varepsilon_{\max,2}). \tag{4.12}$$

The few pairs injected at small ℓ_i add only a perturbation to the photon injection spectrum

$$\frac{\dot{n}_2(\varepsilon)}{\dot{N}} = \frac{\varepsilon_s}{12}\left(\frac{3}{\varepsilon\varepsilon_s}\right)^{3/2}\frac{1}{8z_T}\frac{\ell_i}{\ell_c}\ln\left(\frac{\varepsilon_{\max,2}}{\varepsilon}\right) \qquad (\ell_i \ll \ell_c). \tag{4.13}$$

The perturbation is largest near ε_s and is proportional to ℓ_i as seen in Fig. 6(a) for $\ell_i=0.4$ and 4. When

$$\frac{\ell_i}{\ell_c}\gtrsim\frac{8\tau_T}{\ln(\varepsilon_{max,2}/\varepsilon_s)}\approx\frac{4\tau_T}{\ln(\varepsilon_{max,1})}, \tag{4.14}$$

(where the last expression is $\ll 1$) then even a *small* redistribution of the power at $\varepsilon_{max,1}$ [as $\tau_{\gamma\gamma}(\varepsilon_{max,1})=\ell_i/\ell_c\ll 1$] towards smaller energies will have a *large* effect on the power injected near ε_s. The contribution of the second photon generation increases with increasing ℓ_i until $\ell_i/\ell_c\approx 1$ [see Fig. 6(a) for $\ell_i=40$] at which point pair production starts becoming saturated ($\tau_{\gamma\gamma}\approx 1$) near $\varepsilon_{max,1}$ with $\varepsilon^2\dot{n}_C^{NT}(\varepsilon)=\gamma^2P(\gamma)$ (where $\varepsilon=2\gamma$). Increasing ℓ_i further, causes the injection spectra to approach the saturated solution from Section 3.2 over a larger and larger energy range. $P(\gamma)$ becomes saturated for $\gamma>\varepsilon_{abs}/2$, where $\tau_{\gamma\gamma}(\varepsilon_{abs})=1$, while $\dot{n}_C^{NT}(\varepsilon)$ is saturated for $\varepsilon>\varepsilon_{abs}^2\varepsilon_s/3$. $P(\gamma)$ becomes proportional to $\gamma^{-3/2}$ at all γ and $\dot{n}_2(\varepsilon)$ becomes equal to the saturated solution (equations D2 and D6b) at all ε (i.e. $\varepsilon_{abs}=1$) when

$$\frac{\ell_i}{\ell_c}>2\left(\frac{\varepsilon_{max,2}}{\varepsilon_s}\right)^{1/4}\approx(\varepsilon_{max,1})^{1/2}. \tag{4.15}$$

The partly cancelling effects of down-scatter and diffusion were neglected in our analytical discussion. They only enter when $\tau_T>1$ and affect the final approach to saturation by making $1-\mathscr{E}(2\gamma)$ in equation (4.7) go to unity at a different rate with increasing ℓ_i. Diffusion could be allowed for by multiplying ℓ_i/ℓ_c with $(1+\tau_T/3)$ in all the solutions and by determining τ_T from equations (2.25) and (2.27). The errors made neglecting down-scatter and diffusion are, however, not large as seen in Fig. 6(a).

4.1.2 Opacity feedback from the second photon generation

The pair scattered photons (i.e. the second generation) can contribute to the pair-producing opacity at $\varepsilon_{max,1}$ when $\varepsilon_{max,2}>(\varepsilon_{max,1})^{-1}$. Then equation (4.2a) becomes non-local in the sense that the solution at some photon energies (or Lorentz factors) depends on the solution at other photon energies (or Lorentz factors) with the coupling entering through $\tau_{\gamma\gamma}(\varepsilon)$ in the radiative transfer factor. For Lorentz factors $1<\gamma<(2\varepsilon_{max,2})^{-1}$ and for photon energies $4\varepsilon_s/3<\varepsilon<\frac{1}{3}\varepsilon_s\varepsilon_{max,2}^{-2}$ this does not happen and $P(\gamma)$ and $\dot{n}_2(\varepsilon)$ are still given by equations (4.11) and (4.12), respectively. Now consider a pair particle with a Lorentz factor γ_1 larger than $(2\varepsilon_{max,2})^{-1}$. It is produced by a photon with energy $2\gamma_1$ that has pair produced on a photon at energy $(2\gamma_1)^{-1}$. This target photon is most likely up-scattered from ε_s by a first-generation pair particle of energy $\gamma_2=(8\gamma_1\varepsilon_s/3)^{-1/2}$ which can be shown also to be larger than $(2\varepsilon_{max,2})^{-1}$. Repeating the argument the pair injection at γ_2 depends on the conditions at $\gamma_3=(8\gamma_2\varepsilon_s/3)^{-1/2}$ and so on. The series converges to the Lorentz factor

$$\gamma_c=\tfrac{1}{2}\left(\frac{3}{\varepsilon_s}\right)^{1/3} \tag{4.16}$$

(which has the value 24 when $\varepsilon_s=2.7\times10^{-5}$). A photon at

$$\varepsilon_c=\left(\frac{3}{\varepsilon_s}\right)^{1/3} \tag{4.17}$$

thus produces a pair at γ_c by interacting with a photon that is up-scattered from ε_s by a pair particle of the same Lorentz factor γ_c. This makes the integral equation for $P(\gamma)$ almost local at γ_c and allows for an approximate solution. Using equations (2.13), (2.18), (4.4), and (4.10) and

neglecting diffusion and down-scattering gives (*cf.* equation 4.11)

$$\frac{P_1(\gamma_c)}{\dot{N}}=\frac{1}{4z_T\gamma_c}\left(\frac{\ell_i}{\ell_c}\right)\frac{1+\int_{\gamma_c}^{\gamma_{max,1}}\frac{P_1(\gamma_c)}{\dot{N}}\,d\gamma}{1+\frac{\ell_i}{2\ell_c}\left(\frac{\gamma_c}{\gamma_{max,1}}\right)^{1/2}\left[1+\int_{\gamma_c}^{\gamma_{max,1}}\frac{P_1(\gamma)}{\dot{N}}\,d\gamma\right]}. \tag{4.18}$$

Note that the lower integration limit in the integrals representing the opacity contribution from the second photon generation is precisely γ_c. As $P_1(\gamma)\propto\gamma^{-1}$ until close to saturation the integral can be approximated with $f_1\gamma_c P_1(\gamma_c)$ where $f_1=\max[0, \ln(\gamma_{max,1}/\gamma_c)]$. Close to saturation the integrals in equation (4.18) cancel anyway and the approximation causes no large error. Solving for ℓ_i/ℓ_c gives

$$\frac{\ell_i}{\ell_c}=\frac{4z_T\gamma_c\frac{P_1(\gamma_c)}{\dot{N}}}{\left[1+f_1\gamma_c\frac{P_1(\gamma)}{\dot{N}}\right]\left[1-\frac{P_1(\gamma)}{\dot{N}}\right]}. \tag{4.19}$$

Fig. 7 shows the solutions for $\gamma_{max}=471$ (no opacity feedback, i.e. $f_1=0$) and for $\gamma_{max}=3\times10^3$ including opacity feedback (dashed curve) and neglecting it (solid curve). The figure shows $P_1(\gamma_c)$ as a function of ℓ_i to allow easy comparison with Fig. 8 below. The behaviour of the curves is understandable by examining equation (4.19). When $P_1(\gamma_c)/\dot{N}$ is much less than $(f_1\gamma_c)^{-1}\ll1$ then $\ell_i=\ell_c 4z_T\gamma_c P_1(\gamma_c)/\dot{N}$. When there is no opacity feedback ($\gamma_{max,1}<\gamma_c$) then ℓ_i increases linearly with $P_1(\gamma_c)$ until $P_1(\gamma_c)/\dot{N}$ reaches its saturation value of unity whereupon ℓ_i goes to infinity. When there is opacity feedback ($\gamma_{max,1}>\gamma_c$) then the increase of

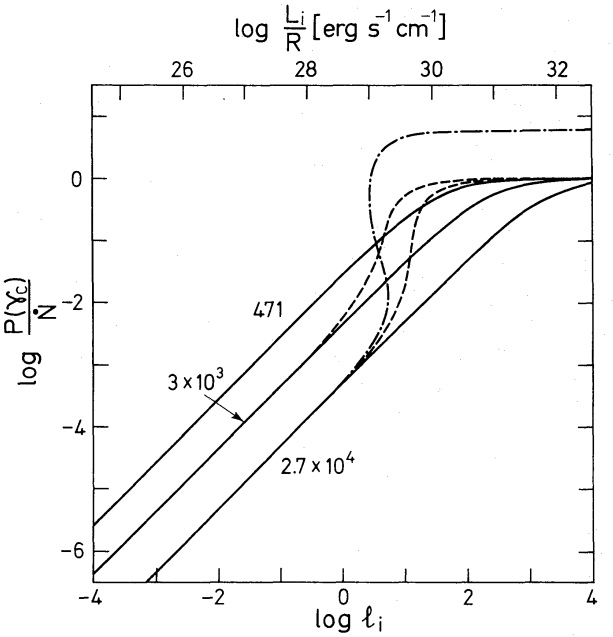

Figure 7. The analytical pair injection rate $P(\gamma_c)$ in terms of the mono-energetic injection rate, $\dot{N}$, as a function of the dimensionless injection compactness ℓ_i or of L_i/R for mono-energetic particle injection at γ_{max}. Soft photons are injected at $\varepsilon_s=2.7\times10^{-5}$ and the curves are labelled by their values of γ_{max}. Opacity and pair-production feedbacks are neglected on the solid curves ($f_1=0$ in equation 4.19), opacity feedback is included on the dashed curves (equation 4.19), and both effects are accounted for on the dashed–dotted curve (equation 4.25).

ℓ_i with $P_1(\gamma_c)$ is suppressed when $P_1(\gamma_c)/\dot{N} > (f_1\gamma_c)^{-1}$ making ℓ_i/ℓ_c start levelling off towards the value $4z_T/f_1$. The saturation factor $1-P_1(\gamma_c)/\dot{N}$ in equation (4.19), however, makes ℓ_i start increasing again as saturation is approached. This levelling off corresponds to the rapid increase of $P_1(\gamma_c)$ which starts near $\ell_i/\ell_c \approx 2z_T/f_1$ as seen in Fig. 7. The most rapid increase occurs at

$$\frac{\ell_i}{\ell_c} = 4z_T\gamma_c \frac{\gamma_c f_1 + (\gamma_c f_1)^{2/3} - (\gamma_c f_1)^{1/3} - 1}{(\gamma_c f_1 + 1)^2} \tag{4.20}$$

which becomes $\ell_i = 5.3$ for $\gamma_{max} = 3\times10^3$ and $\varepsilon_s = 2.7\times10^{-5}$.

A further complication occurs when the second photon generation reaches ε_c (i.e. $\varepsilon_{max,2} > \varepsilon_c$) and can contribute to the pair production at γ_c. The range over which the opacity feedback operates alone at γ_c is determined by the condition $(\varepsilon_{max,1})^{-1} < \varepsilon_{max,2} < (\varepsilon_{max,3})^{-1}$, i.e. when

$$2^{-1/3}(\tfrac{2}{3}\varepsilon_s)^{-2/3} < \gamma_{max} < 2^{-1/6}(\tfrac{2}{3}\varepsilon_s)^{-5/6} \tag{4.21}$$

or $1.2\times10^3 < \gamma_{max} < 8.0\times10^3$ for $\varepsilon_s = 2.7\times10^{-5}$.

Fig. 6(b) shows the full numerical solutions of equations (4.2) for increasing ℓ_i and for $\gamma_{max} = 3\times10^3$ and $\varepsilon_s = 2.7\times10^{-5}$. There is only one secondary pair generation as $\varepsilon_{max,1} = 324$ and $\varepsilon_{max,2} = 0.95$. Equations (4.8) and (4.13) are still valid for small injection compactnesses and from equation (4.13) it is concluded that at $\ell_i \approx 2$ the contribution at ε_s from the second photon generation should equal that of the first (*cf.* the curve $\ell_i = 1$ in Fig. 6b). The rapid increase of $P_1(\gamma)$ and $\dot{n}_2(\varepsilon)$ between $\ell_i = 1$ and 5 is caused by the opacity feedback as discussed above. The analytical results obtained at γ_c agree well with the numerical results for $\ell_i \ll \ell_c$ and near saturation. At intermediate values, say $\ell_i = 5$, the difference is about 30 per cent.

4.1.3 Both opacity and pair-production feedbacks

When $\varepsilon_{max,2} > \varepsilon_c = 2\gamma_c$ then the second photon generation can produce pairs at γ_c. The equivalent condition $\varepsilon_{max,3} > \varepsilon_c^{-1}$ means that the third photon generation contributes to the opacity at ε_c. This situation prevails with increasing γ_{max} until Klein–Nishina effects must be accounted for. The range under consideration is then

$$2^{-1/6}(\tfrac{2}{3}\varepsilon_s)^{-5/6} < \gamma_{max} < (\tfrac{4}{3}\varepsilon_s)^{-1} \tag{4.22}$$

or $8.0\times10^3 < \gamma_{max} < 2.8\times10^4$ for $\varepsilon_s = 2.7\times10^{-5}$.

Let $P_1(\gamma)$, $P_2(\gamma)$, and $P_3(\gamma)$ denote the pair injection rates caused by the first, second, and third photon generation, respectively. $P_3(\gamma)$ contributes the most for γ_{max} near the upper boundary of condition (4.22) (i.e. $z_T = \tfrac{1}{2}$) and for saturated conditions. Fig. 3(b) shows that $P_3(\gamma) < P_2(\gamma)$ for $z > 2\times10^{-5}$. $P_3(\gamma)$ can then be neglected at γ_c for $\varepsilon_s > 3(2\times10^{-5})^{3/2} \approx 3\times10^{-7}$. The integral for $P(\gamma_c)$ in the range given by equation (4.22) when $\varepsilon_s > 3\times10^{-7}$ becomes (*cf.* equation 4.18)

$$\begin{aligned}\frac{P(\gamma_c)}{\dot{N}} &= \frac{P_1(\gamma_c)+P_2(\gamma_c)}{\dot{N}} \\ &= \frac{1}{4z_T\gamma_c}\left(\frac{\ell_i}{\ell_c}\right)\left[1+\int_{2\gamma_c^2}^{\gamma_{max,1}}\frac{P_1(\gamma)}{\dot{N}}\,d\gamma\right] \\ &\quad\times \frac{1+\int_{\gamma_c}^{\gamma_{max,1}}\frac{P_1(\gamma)}{\dot{N}}\,d\gamma+\int_{\gamma_c}^{\gamma_{max,2}}\frac{P_2(\gamma)}{\dot{N}}\,d\gamma}{1+\frac{\ell_i}{2\ell_c}\left(\frac{\gamma_c}{\gamma_{max,1}}\right)^{1/2}\left[1+\int_{\gamma_c}^{\gamma_{max,1}}\frac{P_1(\gamma)}{\dot{N}}\,d\gamma+\int_{\gamma_c}^{\gamma_{max,2}}\frac{P_2(\gamma)}{\dot{N}}\,d\gamma\right]},\end{aligned} \tag{4.23}$$

where the additional integral over $P_1(\gamma)$ represents the pair production at γ_c due to the second photon generation and the new integrals over $P_2(\gamma)$ represent the opacity at ε_c caused by the third photon generation. $P_1(\gamma_c)$ is expected to dominate over $P_2(\gamma_c)$ at $\ell_i \ll \ell_c$ (where equations 4.8 and 4.18 are valid) but is overtaken by $P_2(\gamma_c)$ as ℓ_i increases until saturated conditions are reached where $P_1(\gamma_c)_{sat}/\dot{N}=1$ and where

$$\frac{P_2(\gamma_c)_{sat}}{\dot{N}}=(2\gamma_c)^{1/2}\left[1-\gamma_c\left(\frac{2}{\gamma_{max,1}}\right)^{1/2}\right] \tag{4.24}$$

using the results in Appendix D1. As $P_1(\gamma)\propto\gamma^{-1}$ for small ℓ_i the sum of the opacity integrals over $P_1(\gamma)$ and $P_2(\gamma)$ is approximated with $f_1\gamma_c P(\gamma_c)$ where $f_1=\ln(\gamma_{max,1}/\gamma_c)$. This approximation is correct for small ℓ_i and is wrong by a factor 2 or so at intermediate and large ℓ_i. As in the previous section the error is of no consequence close to saturation. At small ℓ_i where $P(\gamma)\approx P_1(\gamma)\propto\gamma^{-1}$ the pair-production integral over $P_1(\gamma)$ is approximated with $f_2 2\gamma_c^2 P_1(2\gamma_c^2)/\dot{N}\approx f_2\gamma_c P(\gamma_c)/\dot{N}\approx f_2\gamma_c P_1(\gamma_c)/\dot{N}$ where $f_2=\ln(\gamma_{max,1}/2\gamma_c^2)$. Close to saturation the integral becomes equal to $P_2(\gamma_c)_{sat}/\dot{N}$. The integral at any level of saturation is approximated with $\{[f_2\gamma_c P(\gamma_c)]^{-1}+[P_2(\gamma_c)_{sat}]^{-1}\}^{-1}$. Equation (4.23) can then be solved for ℓ_i to give (*cf.* equation 4.19)

$$\frac{\ell_i}{\ell_c}=\frac{4z_T\gamma_c\dfrac{P(\gamma_c)}{\dot{N}}}{\left[1+f_1\gamma_c\dfrac{P(\gamma_c)}{\dot{N}}\right]\left[1+\left\{\left[f_2\gamma_c\dfrac{P(\gamma_c)}{\dot{N}}\right]^{-1}+\left[\dfrac{P_2(\gamma_c)_{sat}}{\dot{N}}\right]^{-1}\right\}^{-1}-\dfrac{P(\gamma_c)}{\dot{N}}\right]}. \tag{4.25}$$

Fig. 7 shows the solution for $\gamma_{max}=2.7\times10^4$ in three cases: (i) neglecting all opacity and pair-production feedbacks (solid curve), (ii) including only the opacity feedback (dashed curve), and (iii) including both effects (dashed–dotted curve). The additional term representing the pair production caused by the second photon generation in the denominator causes ℓ_i not only to level off as $P(\gamma_c)$ increases but to reach a maximum and then to slowly decrease eventually becoming $\propto P(\gamma_c)^{-1}$. Before this happens, however, saturation effects take over making ℓ_i increase again (towards infinity) as $P(\gamma_c)$ approaches $P(\gamma_c)_{sat}$. As seen in Fig. 7 this means that in a narrow range of ℓ_i there are three solutions for $P(\gamma_c)$.

The numerical solutions for $\gamma_{max}=2.7\times10^4$ and $\varepsilon_s=2.7\times10^{-5}$ are shown in Fig. 6(c) for increasing ℓ_i. Near $\ell_i\approx6$ there are three solutions, two of which are stable to perturbations at constant ℓ_i. Fig. 6(c) displays the two stable solutions at $\ell_i=6$. It is evident that small changes in ℓ_i near $\ell_i\approx6$ will cause transitions between marginally pair-dominated states with a small power redistribution towards smaller photon energies and extremely pair-dominated states with very strong power redistribution from higher to lower photon energies. The injection rate at X-ray energies for the low and high state at $\ell_i=6$ differs by the large factor 30.

Deviations from the saturated solution always remain (even for very large ℓ_i) near $\gamma=1$ for $P(\gamma)$ and near $\varepsilon=\varepsilon_s$ for $\dot{n}_C^{NT}(\varepsilon)$. This is caused by the dominance of down-scatter over pair absorption, i.e. $\tau_C(\varepsilon)>\tau_{\gamma\gamma}(\varepsilon)$, for $1<\varepsilon<2$–3.

4.2 THE PAIR YIELD

The pair yield, x, calculated from the numerical solutions using equation (2.25) is shown in Fig. 8 as a function of ℓ_i for the parameters used in Figs 6 and 7. It is of importance to note the similar shapes of the curves $P(\gamma_c)$ versus ℓ_i in Fig. 7 and the curves x versus ℓ_i in Fig. 8. The reason for this correlation is that the level of pair injection at γ_c is an approximative indicator of

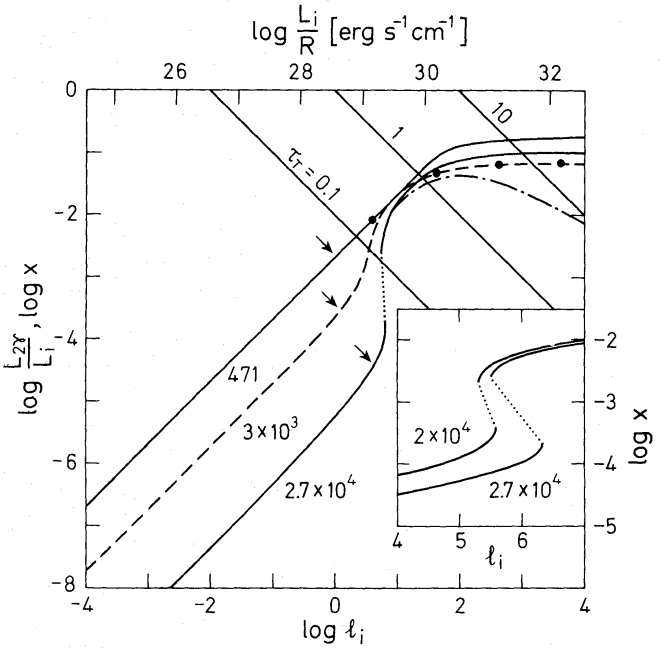

Figure 8. The pair yield, x, as a function of the dimensionless injection compactness ℓ_i or of L_i/R for mono-energetic particle injection at γ_{max}. Soft photons are injected at $\varepsilon_s=2.7\times10^{-5}$ with $\ell_s=4\times10^3$. The arrows mark the points where secondary pair production starts dominating the primary injection. Thomson depths (shown by diagonal lines) are small when pair cascading becomes important. For $\gamma_{max}=2.7\times10^4$ there is a triple-solution region near $\ell_i=6$, which is expanded in the insert, where also the curve for $\gamma_{max}=2\times10^4$ is shown. Expected unstable solutions are indicated by a dotted line. The pair yields approach constant saturation values for large ℓ_i. The dots show the results of F86 for $\varepsilon_s=10^4$ and $\gamma_{max}=10^3$. The dashed–dotted curve shows the ratio of *unscattered* annihilation line luminosity, $L_{2\gamma}$, to injected luminosity, L_i for the case $\gamma_{max}=2.7\times10^4$. Down-scatter reduces the line luminosity for $\tau_T>1$.

the total pair injection, i.e. the pair yield. Thus the features in the pair yield curves are due to the same feedback effects that were responsible for the behaviour of the $P(\gamma_c)$-curves.

The approximate point where the secondary injection becomes of importance is simply when the injection rate of secondary pairs, $x\gamma_{max}\dot{N}\,\mathrm{cm^{-3}\,s^{-1}}$, equals the injection rate of primary particles, $\dot{N}\,\mathrm{cm^{-3}\,s^{-1}}$ (or, equivalently, when the multiplicity equals unity), i.e. when

$$x=\frac{1}{\gamma_{max}}. \tag{4.26}$$

The arrows in Fig. 8 show where this happens. This is also the minimum pair yield needed for the feedback effects caused by secondary pairs to be important.

When there is only one generation and no opacity feedback then using equations (2.25) and (4.11) the pair yield becomes

$$x_1=\left(\frac{\ell_i}{\ell_c}\right)\frac{1}{\varepsilon_{max,1}}\ln\left[\frac{\left(\frac{\varepsilon_{max,1}}{\varepsilon_{min}}\right)^{1/2}+\frac{\ell_i}{2\ell_c}}{1+\frac{\ell_i}{2\ell_c}}\right] \tag{4.27}$$

where diffusion is neglected and the choice of ε_{min} accounts approximately for down-scatter. For $\ell_i\ll\ell_c$ equation (4.27) simplifies into

$$x_1=\left(\frac{\ell_i}{\ell_c}\right)\frac{1}{2\varepsilon_{max,1}}\ln\left(\frac{\varepsilon_{max,1}}{\varepsilon_{min}}\right), \tag{4.28}$$

which in fact is valid at $\ell_i \ll \ell_c$ for all γ_{max} satisfying equation (3.7). For $\ell_i/\ell_c \gg 2(\varepsilon_{max,1}/\varepsilon_{min})^{1/2}$ equation (4.27) reduces to the saturated pair yield as given by equation (3.21).

For the case $\gamma_{max}=471$ and for $\tau_T<1$ equation (4.27) with $\varepsilon_{min}=2$ agrees well with the numerical curve in Fig. 8. At $\tau_T>1$ equation (4.27) with $\varepsilon_{min}=2$ approaches the saturated peak value 0.25, while down-scatter reduces the numerical result to $x_1 \approx 0.18$.

The curve with $\gamma_{max}=3000$ in Fig. 8 represents the case with opacity feedback. Then the increased opacity causes the pair yield to rise rapidly near $\ell_i \approx \ell_c z_T \approx 2.3$ (*cf.* equation 4.20). The pair yield increases by a factor of 10 from 0.1 per cent to 1 per cent while ℓ_i increases by only a factor of about 2.5 (from 2.2 to 5.6). For $\ell_i \gg \ell_c$ the pair yield saturates at 6.6 per cent.

The curves with $\gamma_{max}=2\times10^4$ (the insert) and 2.7×10^4 in Fig. 8 show the additional effects caused by pair-production feedback. There is a narrow range in ℓ_i over which there are three solutions to the cascade problem. The solution that is unstable to constant ℓ_i-perturbations was not determined but the approximate pair yields of this solution are indicated by the dotted curves in Fig. 8. The upper branch solutions were obtained using the pair-dominated cascade solution at larger ℓ_i (outside of the multiple solution range) as a starting point when numerically solving the integral equation. The range over which there are three solutions is $5.5<\ell_i<6.3$ for $\gamma_{max}=2.7\times10^4$ and $5.3<\ell_i<5.6$ for $\gamma_{max}=2\times10^4$ and is expected to disappear for γ_{max} slightly smaller than 2×10^4. Correspondingly there is a range in pair yields that is not realized in stable, steady pair plasmas. This *pair gap* becomes larger with increasing γ_{max} covering more than a decade in x (i.e. the range $2.1\times10^{-4}<x<2.4\times10^{-3}$) for $\gamma_{max}=2.7\times10^4$.

The pair gap occurs for γ_{max} close to ε_s^{-1} ($\gamma_{max} \gtrsim 0.5\varepsilon_s^{-1}$ for the case considered here). For γ_{max} close to ε_s^{-1} the first-order Compton photons can almost reach the energy γ_{max}. They are therefore almost able to pair produce on the mono-energetic soft photons at ε_s. If the soft photon injection at ε_s is not mono-energetic, but has a realistic Wien or Planck shape, then there will be soft target photons available at energies up to a few × the mean soft photon energy. This will change the behaviour of the pair yield curve when $\gamma_{max} \gtrsim 0.3\varepsilon_s^{-1}$, most likely by making $x(\ell_i)$ a monotonically increasing function. This would remove the pair gap.

The dots in Fig. 8 show the pair yields obtained by F86 for the case $\gamma_{max}=10^3$ and $\varepsilon_s=10^{-4}$ [note that $\ell_{Fabian}=(3/4\pi)\ell$]. The pair yield behaves as expected this being a case of one secondary pair generation with opacity feedback but with no pair-production feedback. The numerically obtained saturated ($\ell_i=4000$) pair yields using the solutions of equation (4.2) as well as for the only saturated case in F86 (run 6, $\ell_i \approx \ell_s \approx 4200$) are shown in Fig. 4 by the dashed curve and the dot, respectively. The dashed curve lies somewhat below the analytical $\varepsilon_{min}=2$ curve but above the $\varepsilon_{min}=4$ curve. They would have coincided exactly with the $\varepsilon_{min}=2$ curve had down-scattering been neglected.

Also shown in Fig. 8 are lines of constant Thomson depth using equation (2.27). The Thomson depth τ_T does not become of order unity until the pair yield has reached a level of about 3–4 per cent. The maximum possible Thomson pair depth in Eddington limited plasmas ($\ell_i<4000$) is about 20.

4.3 THE EMERGING SPECTRUM

The spectral shape of the radiation is not the same as that of the injected photon spectrum but it is modified by pair absorption and down-scatter. At an *internal* point this was accounted for by using a modifying radiative transfer factor (see equations 2.15, 2.22, and 2.23). Near the *surface*, however, the radiative transfer effects are different. As the X-ray photon density there suffers no diffusive enhancement the modifying effect of pair absorption is less than at an internal point. In effect, we are dealing with a non-uniform absorbing (photon) medium. Similarly, as hard X-ray photons injected near the surface are likely to diffuse out faster the modifying effects of

down-scatter are also less. Although it is assumed that the photon injection rate, $\dot{n}_C^{NT}(\varepsilon)$, is uniform throughout the cloud (i.e. the solution from Section 4.1 can be used) a different radiative transfer factor, $\mathscr{E}_{esc}(\varepsilon)$ is used to determine the escaping spectrum.

The emerging spectral luminosity at photon energy ε is given by

$$\ell(\varepsilon)=\frac{4\pi}{3}\frac{\sigma_T R^2}{c}\varepsilon\dot{n}_C^{NT}(\varepsilon)\,\mathscr{E}_{esc}(\varepsilon)=\frac{\ell_i}{\gamma_{max}}\varepsilon\frac{\dot{n}_C^{NT}(\varepsilon)}{\dot{N}}\mathscr{E}_{esc}(\varepsilon), \tag{4.29}$$

where $\mathscr{E}_{esc}(\varepsilon)$ is given by equation (2.15) for $\varepsilon>1$ and where the down-scattering effects at $\varepsilon<1$ are prescribed after the results of Sunyaev & Titarchuk (1980) leading to the choice

$$\mathscr{E}_{esc}(\varepsilon)=1-\exp[-(3/\varepsilon\tau_T^2)^{1/2}]. \tag{4.30}$$

This introduces a spectral break of $\Delta\alpha=\frac{1}{2}$ near $\varepsilon_{break}\equiv 1/\tau_T^2$ when down-scatter is important. Note that $\tau_{\gamma\gamma}(\varepsilon)=\eta(3/4\pi)\ell(1/\varepsilon)$ and that

$$\varepsilon\ell(\varepsilon)=\ell_i T(z)\,\mathscr{E}_{esc}(\varepsilon) \tag{4.31}$$

with the cascade function being defined by equation (3.14).

Fig. 9(a)–(c) show sequences of emerging spectra labelled by increasing values of the injection compactness ℓ_i for the same parameter ε_s and γ_{max} as used in Figs 6–8.

In Fig. 9(a), $\gamma_{max}=471$ and $\varepsilon_{max,1}=8$. Pair production takes place close to the threshold and there is only one secondary pair generation. The pair-scattered radiation emerges in the soft X-rays and does not influence the pair absorption. At small ℓ_i the spectral index $\alpha=\frac{1}{2}$ at all photon energies. With increasing ℓ_i pair absorption becomes important above $\varepsilon=1$ and down-scattering steepens the spectrum to $\alpha+\frac{1}{2}\simeq 1$ between ε_{break} (marked by an arrow in Fig. 9a) and $\varepsilon=1$. In the 2–10 keV band α_{2-10} remains close to $\frac{1}{2}$, not being influenced by the pair scattered first Compton radiation. At very large ℓ_i down-scattering steepens α_{2-10} up to a value of 0.8 at $\ell_i=4000$. Additional spectral components (see Section 4.4) may steepen α_{2-10} further.

For $\gamma_{max}=3000$ (corresponding to $z_T\simeq 0.05$) there is also only one secondary pair generation but in this case its scattered radiation extends up to $\varepsilon_{max,2}\simeq 1$. Between $\ell_i=1$ and 5 there is a large change in the X-ray spectrum as part of the injected power near $\varepsilon_{max,1}$ gets redistributed into the X-ray range (*cf.* Fig. 1 in ZL85 where $\ell_i=5$). There is a break at ε_{abs}, where $\tau_{\gamma\gamma}(\varepsilon_{abs})=1$, that moves to smaller photon energies as ℓ_i increases ($\varepsilon_{abs}\simeq 100$ and 5 for $\ell_i=5$ and 40, respectively) and more and more power gets redistributed. α_{2-10} changes from $\frac{1}{2}$ to the value 0.85 (somewhat larger than the value $\frac{3}{4}$ characteristic of the second photon generation, see equation 3.17c). At very large ℓ_i, α_{2-10} steepens further to ≈ 1 due to the influence of down-scatter on cool pairs.

When $\gamma_{max}=2.7\times 10^4$ (corresponding to $z_T\simeq 0.5$) there are three pair generations introducing secondary cascade radiation at almost all photon energies (as $\varepsilon_{max,2}=z_T^2\varepsilon_{max,1}$). The transition across the pair gap near $\ell_i=6$ causes enormous redistribution of injected power. The spectral index α_{2-10} changes from the pre-cascade value of 0.5 to the saturated value of about 0.95 at $\ell_i=400$. The case $\ell_i=20$ with $\alpha_{2-10}=0.85$ is shown in Fig. 2 in ZL85. For larger ℓ_i down-scatter causes α_{2-10} to increase to even larger values ($\alpha_{2-10}>1$). At pair-producing energies the saturated injection spectrum with $\varepsilon\dot{n}(\varepsilon)\propto\varepsilon^{-\alpha(\varepsilon)}$ is reduced by pair absorption to $\ell(\varepsilon)\propto\varepsilon\dot{n}(\varepsilon)/\tau_{\gamma\gamma}(\varepsilon)\propto\varepsilon^{-\alpha(\varepsilon)-\alpha(1/\varepsilon)}$ with $\alpha(\varepsilon)+\alpha(1/\varepsilon)\simeq 0.95+0.95=1.9$ and with $\mathscr{A}(\varepsilon)$ independent of ℓ_i as both $\dot{n}(\varepsilon)$ and $\tau_{\gamma\gamma}(\varepsilon)$ are proportional to ℓ_i.

Fig. 9(a)–(c) show the complexity of the behaviours that are expected when redistribution through pair cascades is important. The generic feature is that redistribution causes most of the injected power to emerge at X-ray energies $[\varepsilon_s<\varepsilon<\min(1,\varepsilon_{max,2})]$. The exact shape of this radiation depends sensitively on the number of pair generations and on the scattering depth τ_T. Only for many overlapping pair generations (more than two) is there a unique spectral shape:

$\alpha \simeq 1$ below $\varepsilon_{\rm break}$ due to energy conservation in the cascade and $\alpha \simeq 1+\frac{1}{2}=\frac{3}{2}$ above $\varepsilon_{\rm break}$ due to down-scatter on cold pairs.

The discontinuity at $\varepsilon=1$ of the non-thermal spectra (solid curves) in Fig. 9(c) is caused by the choices of the radiative transfer factors $\mathscr{E}_{\rm esc}(\varepsilon)$. At $\varepsilon<1$ a gradual flattening is expected near $\varepsilon \simeq 1$ due to the Klein–Nishina decline of the scattering cross-section making down-scatter less important than non-relativistic considerations imply. This enhancement just below $\varepsilon=1$ is partly cancelled by an expected small $[\tau_{\gamma\gamma}(\varepsilon=1)$ is at most a few and decreases rapidly at smaller $\varepsilon]$ but non-negligible $[\tau_{\gamma\gamma}(\varepsilon=1)/\tau_{\rm C}(\varepsilon=1)$ may reach values of 0.3–0.5] amount of pair absorption. Just above $\varepsilon=1$ there is an additional spectral contribution from down-scattered radiation not accounted for here. These effects will fill in the 'valley' apparent near $\varepsilon=1$ when $\ell_{\rm i}$ is large.

Fig. 10 compares the internal and escaping radiation fields. The modifying effects of down-scatter and pair absorption are much larger in the interior of the cloud.

Down-scatter causes a spectral break, $\Delta\alpha$, of unity near $\varepsilon_{\rm break}$ in the interior (making $\alpha \simeq 2$ in

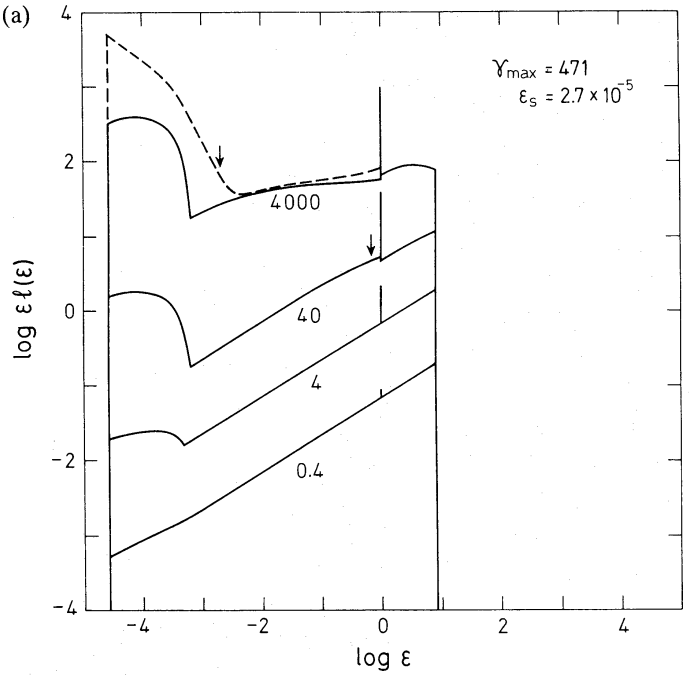

Figure 9. (a) The emerging photon spectrum (shown as the dimensionless spectral luminosity per logarithmic energy interval) as a function of the photon energy ε (in units of mc^2). The non-thermal continua (solid curves) are labelled by the value of the mono-energetic injection compactness $\ell_{\rm i}$ occurring at $\gamma_{\rm max} \approx 471$, while soft photons are injected at $\varepsilon_{\rm s}=2.7\times10^{-5}$ (with $\ell_{\rm s}=4\times10^3$ when determining the pair temperature). The injected photon spectra in Fig. 6(a) have been modified by radiative transfer effects. The first and only secondary pair generation redistributes power from $\varepsilon>1$ to the EUV-band, Compton heating and cooling by cool pairs redistributes power from above $\varepsilon_{\rm break}=\tau_{\rm T}^{-2}$ (shown by arrows) to the soft radiation field at $\varepsilon_{\rm s}$ making a steep power law appear. Additional features are the unscattered annihilation line and down-scattered annihilation photons between $\varepsilon_{\rm break}$ and $\varepsilon=1$. The dashed curve shows the sum of all contributions. $\alpha_{2-10}=0.5$ except at large $\ell_{\rm i}$. (b) Same as (a) but for $\gamma_{\rm max}=3\times10^3$. The injected photon spectra in Fig. 6(b) have been modified by radiative transfer effects. Reprocessing by the one and only secondary pair generation becomes important between $\ell_{\rm i}=1$ and 5. The X-ray spectral index increases from $\alpha_{2-10}=\frac{1}{2}$ at $\ell_{\rm i}=1$ to the expected saturation value $\alpha_{2-10}\approx0.85$ at $\ell_{\rm i}=40$. Down-scatter causes further steepening at larger $\ell_{\rm i}$. The unscattered annihilation line is shown only for $\ell_{\rm i}=1$ and 4000. (c) Same as (a) but for $\gamma_{\rm max}=2.7\times10^4$. The injected photon spectra in Fig. 6(c) have been modified by radiative transfer effects. The runaway pair cascading occurring near $\ell_{\rm i}\approx6$ contains three secondary pair generations. The saturated spectral index $\alpha_{2-10}\approx0.95$ is not reached until $\ell_{\rm i}\approx400$ (*cf.* Fig. 6c). For larger $\ell_{\rm i}$ steepening by down-scatter makes $\alpha_{2-10}>1$. The triangles mark the Compton temperatures of the cold pairs at the cloud surface assuming $\ell_{\rm s}=4\times10^3$. The unscattered annihilation line is not shown for $\ell_{\rm i}=40$ and 400.

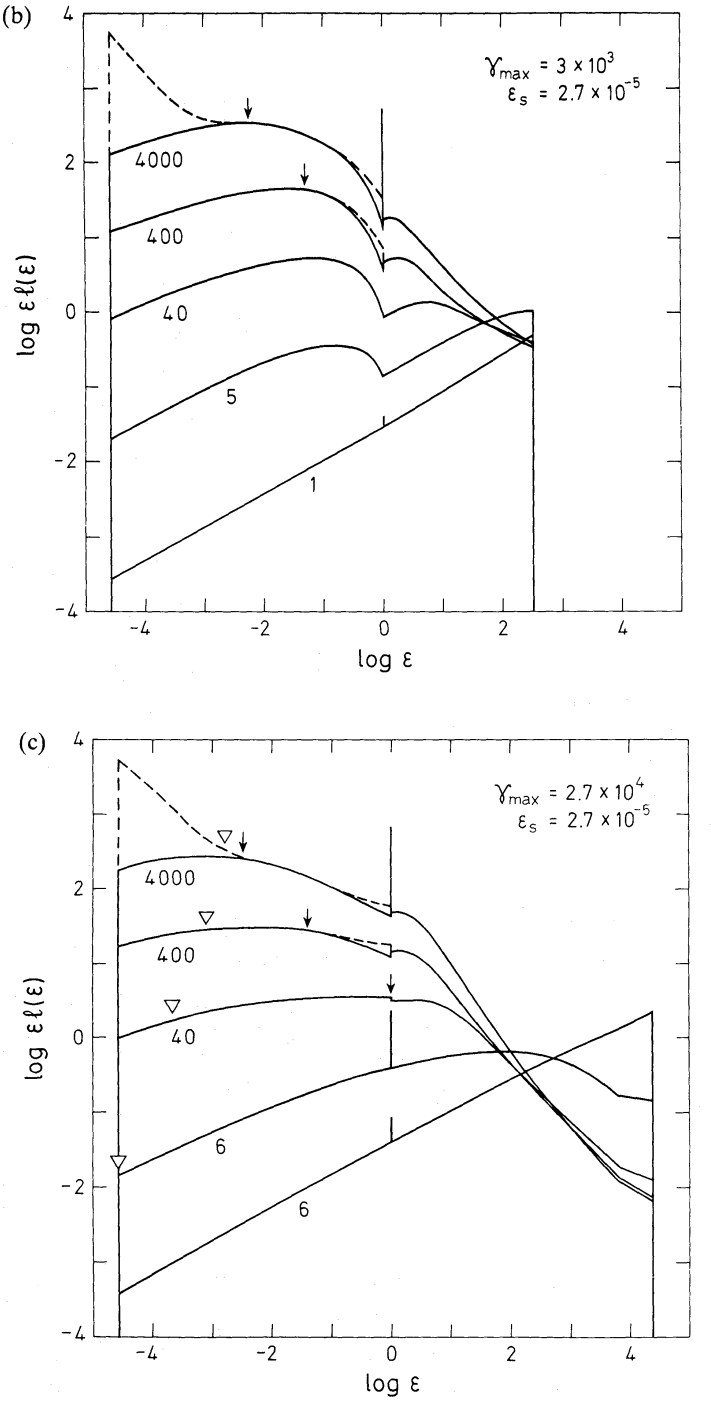

Figure 9–*continued*

the hard X-rays for $\gamma_{max}=2.7\times10^4$) but only by $(\Delta\alpha)_{esc}\approx\frac{1}{2}$ for the escaping radiation. The result, $(\Delta\alpha)_{esc}=\frac{1}{2}$, from Sunyaev & Titarchuk (1980) applies to uniform distributions of scatterers and photon sources. The exact value of $(\Delta\alpha)_{esc}$ in a real inhomogeneous pair cloud is expected to depend on the *relative* distribution of the photon injection and of the cold pairs. As the pairs are made by photons there may exist a rough spatial correlation making $(\Delta\alpha)_{esc}\approx\frac{1}{2}$ in general.

Pair absorption in the interior is a factor $(1+\tau_T/3)$ larger at $\varepsilon>\tau_T^2$ due to the diffusive enhancement at $\varepsilon<\tau_T^{-2}$. The assumption of uniform photon injection is, however, unrealistic.

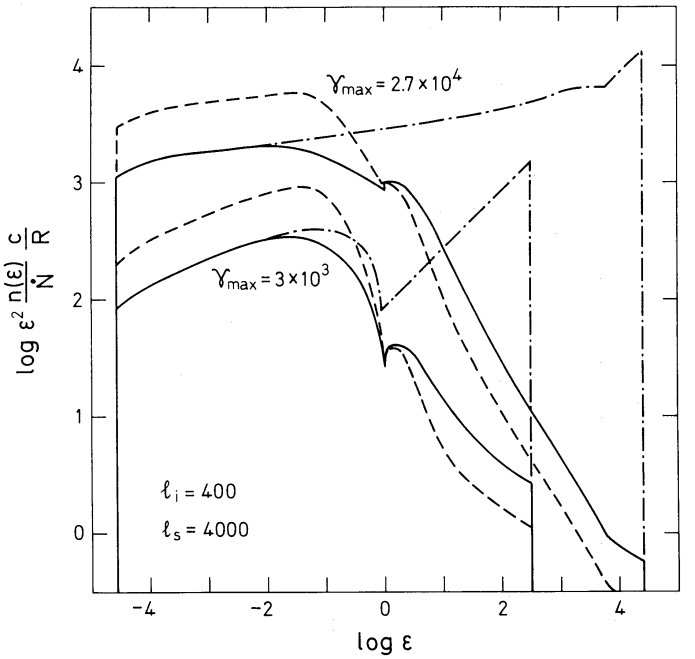

Figure 10. A comparison between the spectral photon densities (shown as the ratio of the spectral energy density per logarithmic energy interval to the primary rest mass injection during a light travel time) in different parts of the cloud for mono-energetic particle injection at γ_{max} and soft photon injection at $\varepsilon_s = 2.7 \times 10^{-5}$. The injected photon spectra, $\dot{n}_C^{NT}(\varepsilon)$, (dashed–dotted curves) are modified by down-scattering and pair absorption to give different spectral shapes in the interior of the pair cloud (dashed curves) and at the surface of the cloud (solid curves). The spectral shape of the escaping radiation is given by the solid curves.

The spatial dependence of the injection of up-scattered soft photons and of the diffusively enhanced density of soft photons at ε_s should be almost the same making the photon injection inhomogeneous for $\tau_T > 1$. The escaping photon density curves at $\varepsilon > 1$ in Fig. 10 may therefore be expected in a more detailed treatment to lie closer to the internal photon density curves. Any pair absorption in the radiation field external to the particle injection region would further degrade the escaping radiation at $\varepsilon > 1$ reducing it by approximately a factor $\exp[-\tau_{\gamma\gamma}(\varepsilon)]$, which can be large at large ε.

4.4 FURTHER SPECTRAL FEATURES

There are additional spectral features stemming from (i) the power converted to pair rest mass, (ii) soft radiation up-scattered by the cold pairs, and (iii) second-order Compton scatterings. The contribution of these spectral components is estimated using the results of the cascade calculations but they were not self-consistently included in those calculations.

4.4.1 Non-scattered 2γ-annihilation photons

The emerging annihilation luminosity written as a compactness is

$$\ell_{2\gamma} = F_{2\gamma} x \ell_i \mathscr{E}(\varepsilon = 1), \tag{4.32}$$

where x is the fraction of injected power ℓ_i converted into pair rest mass, $F_{2\gamma} = (f_a + 0.25 f_{ps})/(f_a + f_{ps})$ ($\simeq 0.8$–0.9 for obtained pair temperatures; see Appendixes C1 and C2 for the annihilation correction factors f_a and f_{ps}) is the fraction of pairs annihilating in 2γ-events, and $\mathscr{E}(\varepsilon = 1)$ (equation 2.15) is the fraction of annihilation photons that escapes suffering neither

down-scatter nor pair absorption. Down-scatter turns out to dominate near $\varepsilon=1$ (see Section 4.1). For $\tau_T<1$ the annihilation photons compactness is $\ell_{2\gamma}\propto\tau_T^2$ (using equation 2.27), while $\ell_{2\gamma}$ is reduced by a factor τ_T making $\ell_{2\gamma}\propto\tau_T$ when $\tau_T>1$ as the unscattered annihilation photons emerge from a surface layer of unit Thomson depth. A convenient expression for the annihilation compactness setting $F_{2\gamma}$ and g_a equal to unity is

$$\ell_{2\gamma}\approx 1.8\tau_T[1-\exp(-0.43\tau_T)]. \tag{4.33}$$

$L_{2\gamma}/L_i$ is shown in Fig. 8 by the dashed–dotted curve for the case $\gamma_{max}=2.7\times10^4$. The reduction due to down-scatter is clearly seen when τ_T becomes larger than unity. Then $L_{2\gamma}/L_i\simeq x/\tau_T\simeq(x/\ell_i)^{1/2}$.

The annihilation spectrum is

$$\ell_{2\gamma}(\varepsilon)=\ell_{2\gamma}\tfrac{4}{3}\varepsilon S_a(\varepsilon), \tag{4.34}$$

where $S_a(\varepsilon)$ is the normalized non-relativistic thermal annihilation spectrum obtained from equation (20) in Svensson (1983). The peak value used in Fig. 9 at non-relativistic temperatures, $\theta\equiv kT/mc^2\ll1$, is $\ell_{2\gamma}(\pi\theta)^{-1/2}$. For the derived Compton temperatures of the cold pairs ($\theta\approx10^{-3}$–10^{-4}, see below) the annihilation line clearly stands out above the continuum for large ℓ_i. However, any bulk or turbulent motion in the pair cloud or any additional pair heating broadens the line tending to make it less visible. The non-thermal continuum level at $\varepsilon=1$ is $\ell(\varepsilon=1)\simeq\ell_i[\tau_T\ln(1/\varepsilon_s)]^{-1}$ including the effect of down-scatter, while the peak of the annihilation line is $\ell_{2\gamma}(\varepsilon=1)\approx\ell_{2\gamma}/(\pi\theta)^{1/2}\simeq x\ell_i/\tau_T(\pi\theta)^{1/2}$. It is concluded that the effective line temperature, θ, needs to be $>0.3(x/0.1)^2[\ln(1/\varepsilon_s)/10]^2$, i.e. mildly relativistic, for the line to get lost in the non-thermal continuum.

It is commonly argued in the literature that an observed ratio of annihilation luminosity, $L_{2\gamma}$, to the integrated luminosity above $\varepsilon=1$, $L(\varepsilon>1)$, of order unity is hard to explain, as there are few hard photons to make pairs and the conversion efficiency (i.e. the pair yield) would have to be unrealistically large. As our discussion has shown, it is natural to expect few photons at $\varepsilon>1$ when strong redistribution through pair cascading takes place. The numerical results show that the ratio $L_{2\gamma}/L(\varepsilon>1)$ reaches saturated values between 0.2 and 1.

4.4.2 Non-scattered 3γ-annihilation photons

The spectral luminosity of non-scattered annihilation photons in the 3γ-continuum from positronium annihilation is approximately

$$\ell_{3\gamma}(\varepsilon)=2\varepsilon F_{3\gamma}x\ell_i\mathscr{E}_{esc}(\varepsilon)\qquad(\varepsilon<1), \tag{4.35}$$

where the factor 2ε gives the approximate normalized distribution (equation C9) and $F_{3\gamma}=0.75f_{ps}/(f_a+f_{ps})$ is the fraction of pairs annihilating in 3γ-events. The ratio of the 3γ continuum to the non-thermal continuum near $\varepsilon=1$ is approximately $2F_{3\gamma}x\ln(1/\varepsilon_s)$, which may not be small compared to unity for small Compton temperatures $\theta<10^{-4}$, where $F_{3\gamma}$ becomes large (>0.3). When $\theta>10^{-3}$, then $F_{3\gamma}<0.1$ and the 3γ-continuum is negligible.

4.4.3 Down-scattered 2γ and 3γ annihilation photons

For $\tau_T\gg1$ most annihilation photons get down-scattered and their continuum makes a substantial contribution to the spectrum between ε_{break} and $\varepsilon=1$. The spectral luminosity is given approximatively by

$$\ell_{down}(\varepsilon)\approx(\varepsilon\tau_T^2)^{-1/2}\tfrac{1}{2}(3-F_{2\gamma})x\ell_i[1-\mathscr{E}(\varepsilon=1)][1-\mathscr{R}(\varepsilon=1)]\qquad(\tau_T^{-2}<\varepsilon<1,\tau_T>1) \tag{4.36}$$

where $x\ell_i$ is the power converted into pair rest mass, $(3-F_{2\gamma})/2$ is the mean number of annihilation photons per mc^2 rest mass, $[1-\mathscr{E}(\varepsilon=1)]$ is the fraction annihilation photons that do not escape before interacting once, while $[1-\mathscr{R}(\varepsilon=1)]$ is the fraction that down-scatters. The first factor describing the spectral shape is based upon equation (30) in Sunyaev & Titarchuk (1980) together with an appropriate normalization factor. Most 3γ-photons are emitted near $\varepsilon=1$ [as $\dot{n}_{3\gamma}\approx\dot{n}_{3\gamma}(\varepsilon=1)$] and are treated in equation (4.36) as originating at $\varepsilon=1$. The ratio of down-scattered annihilation continuum to non-thermal continuum near $\varepsilon=1$ is approximately $x\ln(1/\varepsilon_s)$ (valid when the photon power is evenly distributed, i.e. $\alpha=1$, below $\varepsilon=1$), which is easily of order unity. It is seen in Fig. 9 that the down-scattered annihilation continuum is non-negligible for large ℓ_i.

4.4.4 *Thermally Comptonized soft photons*

The cold thermal pairs are Compton heated by down-scattering the non-thermal continuum and Compton cooled by Comptonizing the soft photons at ε_s. The Compton temperature, θ, of the surface pairs (the interior pairs are somewhat colder) is approximately determined by

$$\theta\approx 0.25\,\frac{\int_{i\varepsilon_s}^{1}\varepsilon\ell(\varepsilon)\,d\varepsilon+\varepsilon_s\ell_s}{\int_{\varepsilon_s}^{1}\ell(\varepsilon)\,d\varepsilon+\ell_s}. \tag{4.37}$$

This is the only place where the soft photon compactness (or luminosity) enters. ℓ_s influences the Compton temperature and thus the correction g_a to the annihilation rate, changing the Thomson depth if the pairs are cold enough. ℓ_s was set to 4000 in the numerical solutions making the Compton temperature increase from $\theta\approx\varepsilon_s/4$ for $\ell_i<\varepsilon_s\ell_s$ up to $\theta\approx\tau_T^{-2}$ for $\ell_i\approx\ell_s$ (see Fig. 9c).

The Comptonized soft photon spectra shown in Fig. 9 for the case $\ell_i=4000$ has spectral indices $\alpha\simeq(9/4+\pi^2/3\theta\tau_T^2)^{1/2}-1.5$ and may cause a large steep contribution in the soft X-rays.

4.4.5 *Second-order Compton scattering*

The ratio of first-order Compton scattered injection spectra to the primary injection rate, $\dot{n}_C^{NT}(\varepsilon)/\dot{N}$, does not depend in an apparent way on the hard and soft injection rates [see e.g. equation (2.19) or (3.1)].

In Appendix E the second-order Compton scattered injection spectrum is calculated analytically for the case of saturated pair production with mono-energetic particle injection. Down-scattering of first-order photons was neglected. Fig. 11(a) and (b) show the first- and second-order Compton scattered injection spectra for the same values of γ_{max} and ε_s as in Figs 6–10.

As shown in Appendix E, the ratio of the second-order Compton scattered injection spectrum to the primary injection rate depends on $(R/c)(\dot{N}/n_s)\propto L_i/L_s$, i.e. on the ratio of the injected particle luminosity to the soft luminosity. When the soft luminosity dominates, then the second-order Compton radiation is negligible. In Fig. 11(a) and (b) the ratio L_i/L_s is set to unity. The Klein–Nishina cut-off generally causes the second-order spectrum to peak at ε of order unity. Fig. 11(a) shows that when the generations are well separated (i.e. z_T is small) then the second-order photons make a non-negligible contribution in the 'valleys' of the first-order spectrum. When the generations overlap (i.e. z_T of order unity) then Fig. 11(b) shows that second-order photons are only marginally important near $\varepsilon=1$ for $L_i/L_s=1$. The negligence of down-scattering overestimates the contributions near $\varepsilon=1$. It is concluded that the second-order

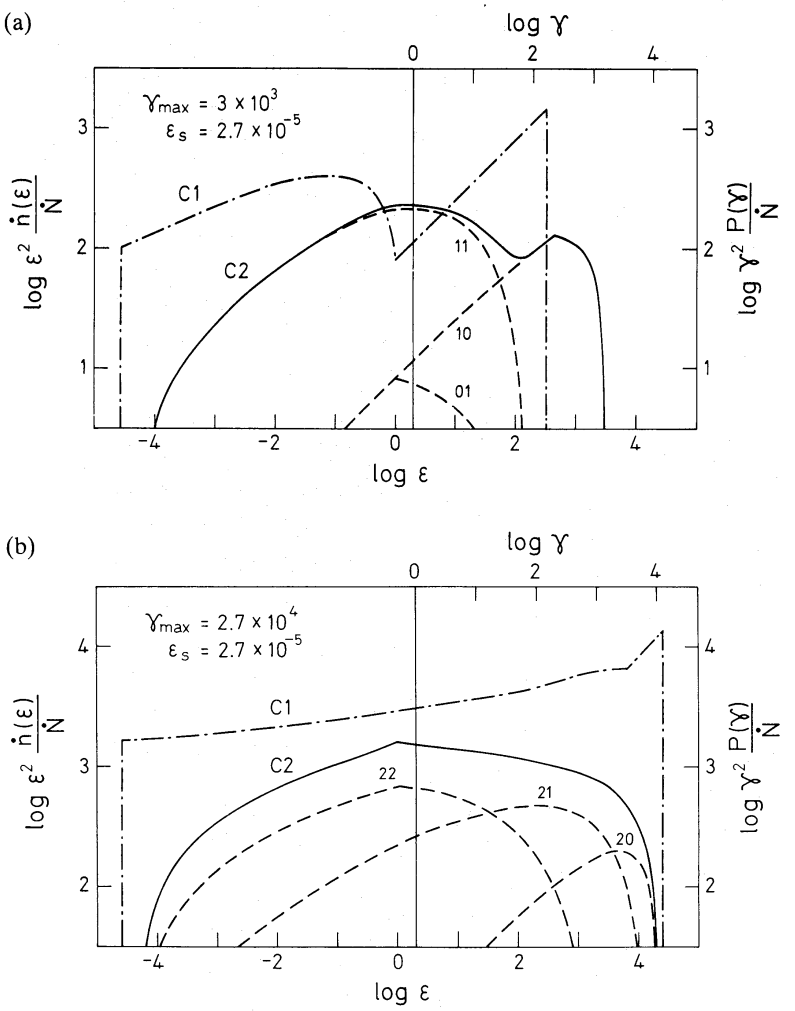

Figure 11. (a) The injected photon spectra of first- and second-order Compton scattered photons for the case of saturated pair cascades with a particle power L_i injected mono-energetically at γ_{max} and a soft photon power L_s injected at ε_s. The first-order Compton spectrum denoted by C1 (dashed–dotted curves) is the same as the saturated injection spectrum in Fig. 6(b). The second-order Compton spectrum denoted by C2 (solid curve) scales *linearly* with L_i/L_s ($L_i/L_s=1$ in the figure) and consists of four components (dashed curves) as there is only one secondary pair generation. The components are marked by two digits, *km*, indicating that the photons first scatter on the *k*th pair generation and then on the *m*th generation. 0 denotes the primary particles. See Appendix E for details. (b) Same as (a) but for a case with three secondary pair generations and $(1+3)^2=16$ second-order components, three of which are shown (dashed curves). The first-order Compton spectrum (dashed–dotted curve) is the same as the saturated injection spectrum in Fig. 6(c).

photons can be safely neglected for $L_i/L_s \leq 0.1$. The solutions of this paper are expected to be approximately true even for L_i/L_s of order unity (in particular for z_T of order unity) as second-order photons are only marginally important and as down-scattering reduces the effect the first-order photons otherwise would have had on the particle cooling. Finally, it is evident from Fig. 11 that with an increasing second-order contribution the X-ray spectral slope, α_{2-10} will decrease.

5 Previous work

There are some further comments to be made concerning previous work treating pair cascades for the *same* case as considered here (i.e. mono-energetic or power law [with $\Gamma<2$] injection of particles with a power L_i interacting in the Thomson limit with external soft photons of power L_s,

where $L_i/L_s<1$). The relevant work (see Table 1) is by Kazanas (1984), ZL85, and F86. The approaches in these papers are all the same in the sense that the kinetic equations are considered at some representative internal point in the pair cloud.

Kazanas (1984) obtained analytical solutions for *saturated* pair cascades setting $\mathscr{E}(\varepsilon)=\Theta(\varepsilon_{\min}-\varepsilon)$ implying that *all* photons above $\varepsilon_{\min}$ pair produce, but none below (Θ is the Heaviside step function). Kazanas' resulting $N(\gamma)$ is in disagreement with our analytical solutions for reasons given in Section 3.3. Kazanas also gives a qualitative steady-index argument for why the steady particle spectrum becomes a power law with $N(\gamma)\propto\gamma^{-3}$. The scattered photons then have the spectral index $\alpha=1$. The steady-index argument can be put on a firmer quantitative basis by considering equation (3.6) at a z-value where neither the primary injection nor the highest generation contributes. Denoting the sum over the generations by $S(z)$ gives

$$S(z)=\tfrac{1}{2}z^{-3/2}\int_{z^{1/2}}S(z')\,dz'. \tag{5.1}$$

Assuming the solution to be a power law, $S(z)=S_0z^{-1-\alpha}$, with $\alpha>0$ means that the upper integration limit can be neglected. Integrating and equating the left- and right-hand side exponents gives $\alpha=1$. This is the argument of Kazanas. Equating the coefficients, however, gives $\alpha=1/2$. Thus, there is no power law solution of equation (5.1). The steady-index argument also fails due to the limited number of generations in Thomson cascades. Only close to the Klein–Nishina limit (i.e. for z_T of order unity) do three or four generations overlap sufficiently to produce a smooth-looking spectrum with α slightly less than unity. The reason for this, as argued in Section 3.2, is simply approximate energy conservation from one generation to the next.

As our formulation of the cascade problem is an extension [i.e. including down-scatter in $\mathscr{E}(\varepsilon)$] of that of ZL85, the results where overlap occurs (i.e. for $\tau_T<1$) are in excellent agreement.

F86 solve the time-dependent kinetic equation for the photon distribution numerically. This allows exploration of both time-dependent and steady aspects of non-thermal pair plasmas. The steady solutions discussed by F86 have $\tau_T>0.2$ and are thus dominated by secondary pairs (see Fig. 8). All *displayed* solutions have $\varepsilon_{\max,2}<1$ and first-order photons thus only make *one* secondary pair generation. As noted in Section 3.2, the characteristic index of the second photon generation at small photon energies is $\alpha=3/4$, accounting partly for the prevalence of this index in F86.

The emergent spectra determined by F86 are in rough overall agreement with the emergent spectra presented here having spectral breaks at $\varepsilon_{\text{break}}$ and $\varepsilon\approx1$ for large ℓ_i. There are differences in details, however, for the following main reasons:

(i) The treatment of down-scatter in F86 is valid for the internal radiation field giving a spectral break $\Delta\alpha\approx1$ at $\varepsilon_{\text{break}}$ instead of $(\Delta\alpha)_{\text{esc}}\approx1/2$.

(ii) The escape term used by F86 corresponds to a radiative transfer factor $\mathscr{E}(\varepsilon)=[1+(1+\tau_T)\,\tau_{\gamma\gamma}(\varepsilon)]^{-1}$ at $\varepsilon>1$. As $\tau_{\gamma\gamma}(\varepsilon)$ was calculated using the diffusively enhanced internal photon density, their spectra at $\varepsilon>\tau_T^2$ is expected to be reduced by a factor $(1+\tau_T)^2$ relative to those presented here in Fig. 9. The different $\mathscr{E}(\varepsilon)$ used causes the *unsaturated* pair and photon injection spectra to differ.

(iii) F86 treated the cases $L_i/L_s=1$ and 10 necessitating the inclusion of higher-order Compton scatterings in their work. The second-order Compton radiation when important tends to flatten the injected X-ray spectra (see Section 4.4.5 and Zdziarski & Lamb 1986).

6 Observable properties and variability of compact X-ray sources

6.1 OBSERVATIONS

The assumption of a dominant soft luminosity $L_s>L_i$ limits the observational considerations to objects that are relatively strong at softer energies. This is the case for the many Seyfert 1-galaxies

and quasars that exhibit a UV-bump (e.g. Edelson & Malkan 1986; Elvis *et al.* 1986) and where even more soft power may be hidden in the unobserved EUV-band. There are presently three main observables in the X-ray range in these objects: (i) the luminosity L in some spectral range (e.g. 2–10 keV), (ii) the spectral slope α of a power law fit in this spectral range, and (iii) the time variability, Δt, of the integrated flux in the same spectral range. The observed compactness is defined as

$$\ell_{2-10}^{\text{obs}} = \frac{L_{2-10}}{c\Delta t}\frac{\sigma_{\text{T}}}{mc^3}, \tag{6.1}$$

where the light travel-time distance, $c\Delta t$, provides an upper limit to the actual source size. It is therefore expected that ℓ_{2-10}^{obs} is a lower limit of the true compactness, ℓ_{2-10}, of the same source, i.e.

$$\ell_{2-10} > \ell_{2-10}^{\text{obs}}. \tag{6.2}$$

The most rapid time variability may give ℓ_{2-10}^{obs}-values close to the true ℓ_{2-10}.

The X-ray *spectral* properties of active galactic nuclei are reviewed in Elvis & Lawrence (1985). The spectral slope, α, for hard X-ray selected active galaxies (mostly Seyfert 1 galaxies were observed) seems to cluster around a 'universal' value of 0.7 in the spectral range, 0.75–120 keV, covered so far (see Elvis & Lawrence 1985 and references therein). The few studied QSOs, to the other hand, show a greater spread with α ranging from 0.6 to 2.3 in the spectral range 0.2–3 keV with a mean value of about 1. The possibility exists that QSOs are similar to BL Lacs in having a steep soft component and a hard (possibly 'universal') component. The observed value of α then depends on at which photon energy the break-point between the two spectral components occurs. Observations of NGC 4151 (Perola *et al.* 1986) contradicts the existence of 'universal' spectral index for Seyfert 1 galaxies. They found a correlation between $\alpha_{3.5-25}$ and L_{2-10} with a $\alpha_{3.5-25}$ increasing from 0.2 to 0.7 as L_{2-10} increases by a factor of 5. Thus, NGC 4151 has at low luminosities a spectrum that is much harder than the 'universal' spectrum.

Barr & Mushotzky (1986) compiled luminosity and fastest *time variability* data for 28 objects (Seyferts 1s, QSOs, and BL Lacs). For the sample of Seyferts and QSOs they found the correlation $L_{2-10} \propto (\Delta t)^{0.9\pm0.2}$ implying $\ell_{2-10}^{\text{obs}} \approx$ constant. A histogram of the distribution in $\log \ell_{2-10}^{\text{obs}}$ for the 28 objects (see Fabian 1987) show a large peak at $\ell_{2-10}^{\text{obs}} \approx 0.1-0.3$. This peak consists almost exclusively of Seyfert 1 galaxies. Excluding NGC 6814, whose rapid time variability (100 s) may be due to Earth-related phenomena (Beall, Wood & Yentis 1986) we find that the remaining 11 Seyfert 1s have the mean value $\langle \log \ell_{2-10}^{\text{obs}} \rangle = -0.85 \pm 0.4$. Barr (1986) reported that ℓ_{2-10}^{obs} in the Seyfert galaxy NGC 4593 varied much less than L_{2-10} implying a correlation between L_{2-10} and the size R of the source.

So while the compactness ℓ_{2-10}^{obs} falls in a narrow range for the sample with known time variability as well as for one well-observed Seyfert 1 galaxy the situation is less clear as regards the spectral index α. NGC 4151 has at times a very hard spectrum and the sample with known (i.e. rapid) time variability seems to exhibit a larger dispersion in α_{2-10} than what is the case for all Seyfert 1 galaxies with known α_{2-10}. Perhaps the 'universal' index is characteristic for objects in their quiescent state.

A limited number (11 in the sample of Rothschild *et al.* 1983) of active galactic nuclei have spectral information up to 120 keV and only a handful have been observed beyond that. Upper limits or possible detections in the MeV-range show that objects such as NGC 4151, MCG 8-11-11, Cen A, and 3C 273 must have a spectral break at a few MeV (see Bezler *et al.* 1984 and the data compilation in Bassani & Dean 1983; Bassani *et al.* 1985). The cosmic X- and γ-ray backgrounds also require most active galaxies to turn over in the MeV-range or below (Rothschild *et al.* 1983).

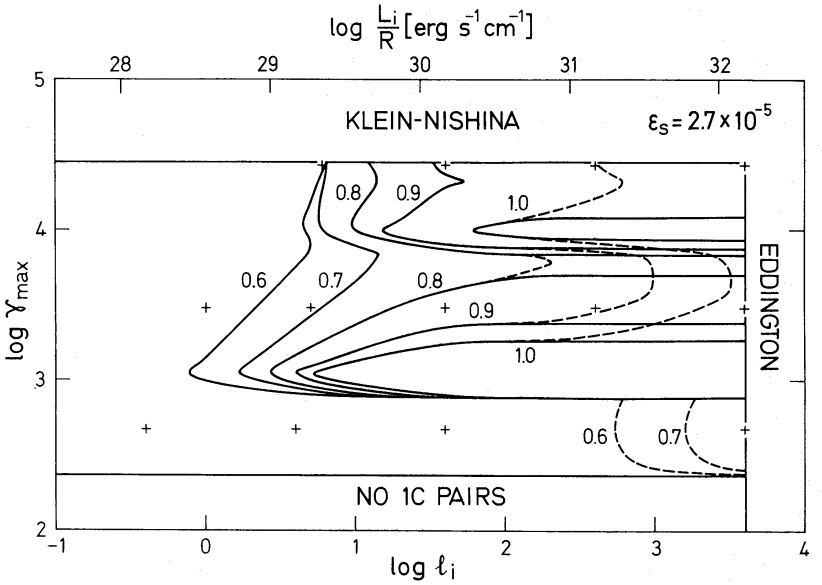

Figure 12. Isocontours of constant spectral index, α_{2-10}, for the 2–10 keV band in parameter space (γ_{max}, ℓ_i) at constant $\varepsilon_s = 2.7 \times 10^{-5}$. The parameter space is limited by the Thomson limit condition $4\gamma_{max}\varepsilon_s/3 < 1$, by the pair–free Eddington limit $\ell_i < \ell_{Edd} = (2\pi/3)(m_p/m)(3R_g/R) < (2\pi/3)(m_p/m) \approx 4000$, and by the condition (see equation 2.6) required for first-order Compton photons to be able to produce pairs. Only isocontours with $\alpha_{2-10} < 1$ are shown with each contour being marked by its value of α_{2-10}. Solid curves neglect while dashed curves include down-scatter by cold pairs. The plus signs mark the parameters of the emerging spectra displayed in Fig. 9(a)–(c). The observed 'universal' index, $\alpha_{2-10} = 0.7$, occur in a vertical strip with $\ell_i \approx 3$–10.

6.2 2–10 keV PROPERTIES OF PAIR CASCADES

Figs 12 and 13 show the spectral slope defined as

$$\alpha_{2-10} \equiv \frac{\log[\ell(\varepsilon = 2\,\mathrm{keV})/\ell(\varepsilon = 10\,\mathrm{keV})]}{\log 5} \tag{6.3}$$

and the compactness

$$\ell_{2-10} \equiv \int_{2/511}^{10/511} \ell(\varepsilon)\, d\varepsilon \tag{6.4}$$

calculated using $\ell(\varepsilon)$ from equation (4.29) and the numerical solutions of equations (4.2). The results are displayed as isocontours of constant α_{2-10} and ℓ_{2-10} in the parameter space (γ_{max}, ℓ_i) keeping ε_s fixed at 2.7×10^{-5}.

In Fig. 12 the isocontours are labelled by their values of α_{2-10}. The solid contours neglect down-scatter while the dashed contours show the steepening effect of including down-scatter by the cold pairs. The mechanisms broadening the annihilation line (see Section 4.4.1) would make the true isocontour lie somewhere in between these extreme cases. When there is no or little pair production ($\ell_i \ll 1$) or when $\varepsilon_{max,2} < 2$ keV then $\alpha_{2-10} = 0.5$. When there is power redistribution through pair cascades *and* $\varepsilon_{max,2} > 2$ keV then α_{2-10} increases. The close contours near $\gamma_{max} \approx 8 \times 10^2$ and 8×10^3, and the kinks at $\gamma_{max} \approx 2 \times 10^4$ are caused by the second, third, and fourth photon generation entering the 2–10 keV range with increasing γ_{max}. The merging of the $\alpha_{2-10} = 0.6$ and 0.7 contours for large γ_{max} is due to the pair runaway at $\ell_i \approx 6$ (see Sections 4.1.2 and 4.2).

In Fig. 13 the regions in parameter space with little pair production or with $\varepsilon_{max,2} < 2$ keV are characterized by diagonal isocontours as $\ell_{2-10} \propto \ell/\gamma_{max}$ in these regions. There is a sharp kink in

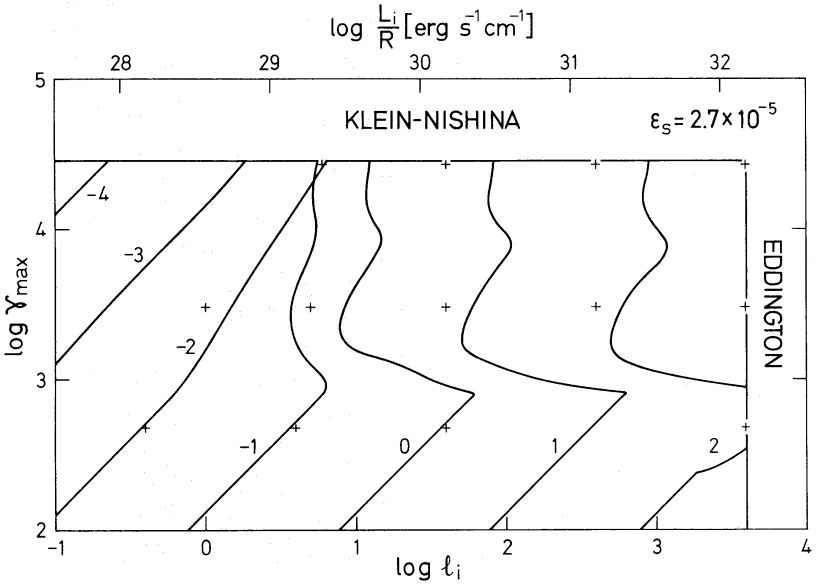

Figure 13. Same as Fig. 12 but shows isocontours of constant compactness, ℓ_{2-10}, in the 2–10 keV band. The contours are marked by their values of log (ℓ_{2-10}). The observed compactness, $\ell_{2-10}^{obs} \approx 0.1-0.3$, occurs in a vertical strip with $\ell_i \approx 3-10$.

the contours at the point where $\varepsilon_{max,2}$ becomes larger than 2 keV. At larger values of γ_{max} at a given large $\ell_i (\gtrsim 10)$ pair cascades redistribute an almost constant (i.e. independent of γ_{max}) fraction of the injected power into the 2–10 keV range making the ℓ_{2-10}-contours almost vertical. This corresponds to the approximately constant pair yield in saturated or nearly saturated conditions (see Fig. 4).

The 2–10 keV properties change rapidly for small variations in ℓ_i and γ_{max} in regions in parameter space with sharp features and close contours. These features as well as the regions with $\alpha_{2-10} > 1$ will, however, disappear or at least become less conspicuous when L_i approaches L_s as then higher order Compton scatterings become important smoothing out the responsible sharp features in the spectrum (Section 4.4.5).

In pair cascades in dominant soft radiation fields, the 'universal' index $\alpha_{2-10} \approx 0.7$ and $\ell_{2-10} \approx 0.1-1$ (i.e. the observed values) occur in an approximately vertical strip in parameter space (γ_{max}, ℓ_i) with γ_{max} large enough to make $\varepsilon_{max,2} > 10$ keV and with $3 \lesssim \ell_i \lesssim 10$. This is the region where redistribution through pair cascades is important but where neither saturated nor Thomson thick conditions occur. There appears to be nothing in the cascade mechanism itself that can lock sources in this region of parameter space. The answer as to why sources occupy this strip may lie in considering radiation-hydrodynamical and injection feedback effects. If the particle injection and the pair cascading take place in the relatively proton free coronas or funnels of accretion discs, then the pair Eddington limit is approximately $\ell_{Edd}^{pair} = (2\pi/3)(3R_g/R) < 3$. As $\ell_s > \ell_i$ was assumed, ℓ_s (as well as ℓ_i) in the parameter strip exceeds the pair Eddington limit making radiation pressure drive a pair wind (or jet). This will supply seed pairs for the possible release of stored (magnetic) energy at larger radii causing both the injection luminosity and the size of the injection region to increase. Such a feedback causes L_i and R to correlate possibly making ℓ_i have an upper limit of a few $\times 2\pi/3 \approx 10$.

The longest time-scale involved in achieving a steady state of a saturated pair cascade is the diffusive escape time for X-ray photons, $(1+\tau_T) R/c > R/c$, as the cooling time (also being the photon production time), $(R/c)(\ell_s \gamma)^{-1} < R/c$, and the pair-production time-scale, $(R/c)\,\tau_{\gamma\gamma}(\varepsilon)^{-1} < R/c$, are less. For unsaturated cascades having $\ell_i \approx 1-10$, the Thomson depth is

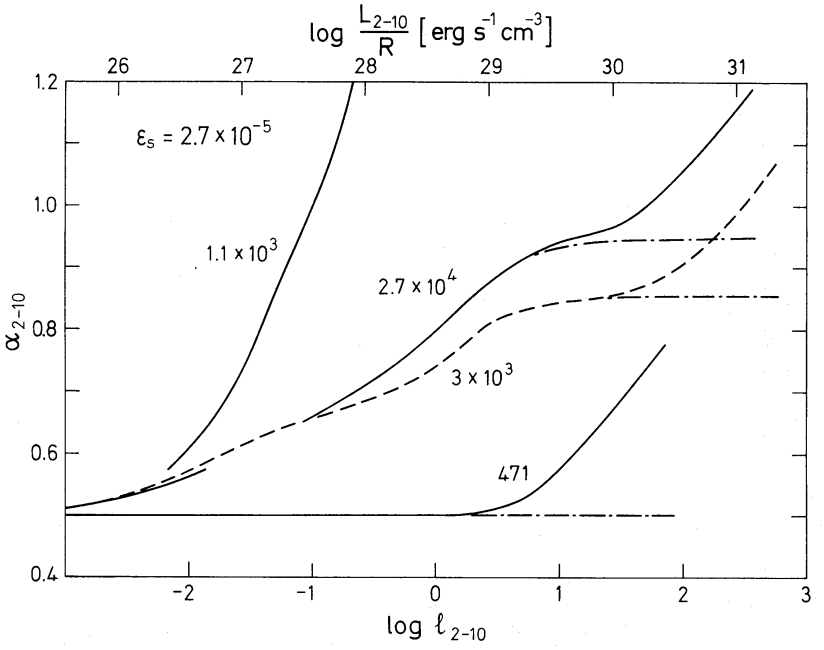

Figure 14. The spectral index α_{2-10} versus the compactness ℓ_{2-10} in the 2–10 keV band when changing ℓ_i at constant γ_{max} and ε_s. The curves are labelled by their values of γ_{max}, while $\varepsilon_s = 2.7 \times 10^{-5}$. Dashed–dotted curves neglect the effects of down-scatter by cold pairs. Note the 'pair gap' of the curve for $\gamma_{max} = 2.7 \times 10^4$.

less than unity and $\tau_{\gamma\gamma}(\varepsilon)$ is less than unity below some photon energy ε_{abs} (see Section 4.1.1). Here, steady state at $1 < \gamma < \varepsilon_{abs}/2$ and $\varepsilon_s < \varepsilon < \varepsilon_{abs}^2 \varepsilon_s/3$ is approached only after a time-scale $(R/c)\tau_{\gamma\gamma}(\varepsilon)^{-1} > R/c$. As the source variability due to changes of details in the power injection or due to changes in the source size can be as rapid as R/c it may be that steady state is not always achieved at small Lorentz factors and at soft photon energies.

Sources varying slow enough may be represented as moving along a sequence of steady states in the parameter space (ε_s, γ_{max}, ℓ_i). Keeping ε_s constant (e.g. the mean photon energy of the UV-bump and/or the temperature of an accretion disc) this corresponds to the source moving around in Figs 12 and 13 and the values of α_{2-10} and ℓ_{2-10} can be determined along the track. Two special cases exist: varying ℓ_i at constant γ_{max} or varying γ_{max} at constant ℓ_i.

Fig. 14 shows how α_{2-10} and ℓ_{2-10} change as ℓ_i varies at constant γ_{max} and ε_s. Besides displaying the curves for the γ_{max}-values of Figs 6–10 the curve for $\gamma_{max} = 1.1 \times 10^3$ (at which the steep upper cut-off of the second photon generation appears in the 2–10 keV window) is also shown. On the dashed–dotted curves down-scatter is neglected. The general behaviour is a slowly increasing α_{2-10} with increasing ℓ_{2-10} at γ_{max}-values where redistribution through first-order Compton cascades occurs. α_{2-10} reaches the analytical saturation values for the injected photon spectrum at $\ell_{2-10} >$ a few (dashed–dotted curves). However, at approximately the same point down-scatter affects the escaping spectrum making α_{2-10} increase further.

Fig. 15 shows how α_{2-10} and ℓ_{2-10} change as γ_{max} varies at constant ℓ_i and ε_s. Results are displayed for $\ell_i = 6$, 10, and 40. There is a characteristic cork screw behaviour with γ_{max} increasing clockwise along the curve. α_{2-10} is equal to ½ at small γ_{max}, but at larger γ_{max} where the second photon generation enters the 2–10 kev band there is a sharp increase in α_{2-10}. As the upper cut-off of the second photon generation moves out of the 2–10 keV band, the value of α_{2-10} decreases again until the third photon generation enters the 2–10 keV band at which point there is a sharp increase again. At the last minimum the fourth photon generation enters the 2–10 keV range. At nearly saturated conditions ($\ell_i \approx 40$) it is seen in Fig. 15 that the minima almost reach down to the saturated asymptotic low-energy spectral indices, $\alpha_2 = 3/4$ and $\alpha_3 = 0.875$ (see Section 3.2). The

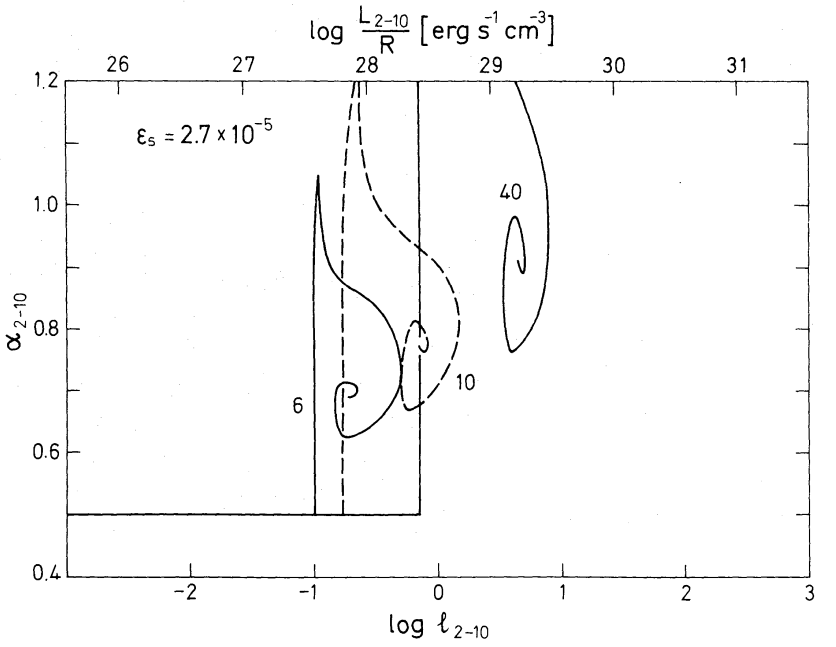

Figure 15. Same as Fig. 14 but for the case when γ_{max} changes keeping ℓ_i and ε_s constant. The curves are labelled by their values of ℓ_i, while $\varepsilon_s = 2.7 \times 10^{-5}$. γ_{max} reaches its largest value (consistent with the Thomson limit assumption) at the centre of the corkscrew-shaped curves.

inclusion of second-order Compton scatterings when L_i approaches L_s would decrease the α_{2-10}-amplitude of the cork screw and would remove the sharp peaks and breaks.

The few detailed observations available for single objects indicate a fairly constant ℓ_{2-10}^{obs} (NGC 4593) and large changes in α_{2-10} when L_{2-10} is varying (NGC 4151). If *both* of these characteristics occur in the same object, such objects would move within a narrow vertical strip in the α_{2-10}–ℓ_{2-10}-plane making γ_{max}-variations rather than ℓ_i-variations to be the most likely cause for rapid variability. It is, however, clear that pair cascade models with $L_i < L_s$ cannot account for $\alpha_{2-10} < 1/2$ as has been observed in, e.g. NGC 4151.

Cavaliére (1982) discussed the feedback non-thermal pair production would have on the particle acceleration (and injection). The pairs would increase the number of particles available for reacceleration, possibly increasing the number of particles being accelerated. Each particle would then get a lower γ_{max} if the injected power remains the same. Further multiplication of the particle number due to the cascade would reduce the mean γ_{max} further until either the particle acceleration mechanism is quenched (e.g. the electric fields being short-circuited) or a pair-production threshold is reached. In the case treated here ($L_i \ll L_s$) such a threshold is reached when γ_{max} becomes of the order of $\varepsilon_s^{-1/2}$ (i.e. $\varepsilon_{max,1} \approx$ a few), while for $L_i > L_s$ higher order Compton scattered photons may make the degradation of γ_{max} continue until γ_{max} is on the order of a few. When the particle acceleration is quenched or the energy supply runs out the cascading stops, the pairs annihilate, and the process may start all over again with a few particles being injected at some large γ_{max}.

On the basis of the above discussion we speculate that feedback on the acceleration mechanism (making γ_{max} vary) and feedback due to radiation pressure (making ℓ_i have an upper limit) are possible causes for the observed values and behaviour of α_{2-10} and ℓ_{2-10}.

The required spectral break at a few MeV is difficult to explain within the models with $L_i < L_s$ as for $\ell_i < 10$ the smooth turnover due to pair absorption occurs at large $\varepsilon_{abs} > 100$ (unless $\varepsilon_{max,1} < \varepsilon_{abs}$; see Fig. 9b and c). As was discussed above, feedback on the acceleration mechanism naturally produces small $\varepsilon_{max,1}$ ($\approx$ a few) with a (sharp) spectral break at $\varepsilon_{max,1}$. Then, however,

$\alpha_{2-10}\approx\frac{1}{2}$ for $L_i \ll L_s$ (Fig. 9a), which disagrees with the observed α_{2-10}. It is clear that the effects the higher order Compton scatterings have on α_{2-10} when $L_i \approx L_s$ need to be explored.

7 Discussion

Improvements of our treatment of pair cascades are needed in at least three areas: radiative transfer, radiation hydrodynamics and particle acceleration. For large injection compactnesses, the emerging radiation is coming from optically thick surface layers and only detailed radiative transfer calculations can provide reliable spectra (at least at $\varepsilon>1$). The Eddington limit is more easily reached once secondary pairs are present and radiation pressure effects will invalidate the assumption of a static cloud. As the secondary pairs can also be accelerated there is probably a strong feedback on the acceleration mechanism making the easily parametrized ($\dot{N}$, γ_{max}, and Γ) injection assumption to be too simplistic. With this in mind, we briefly discuss the expected results of extending our approach to the regions of parameter space, $\gamma_{max}\varepsilon_s>1$ and $L_i>L_s$, where cascades of type I and III reside.

7.1 KLEIN–NISHINA CASCADES ($\gamma_{max}\varepsilon_s>1$)

When $\gamma_{max}\varepsilon_s>1$, then up-scattered photons at energies $>\varepsilon_s^{-1}$ can pair produce on the soft photons at ε_s. The opacity at $\varepsilon>\varepsilon_s^{-1}$ very approximately becomes $\tau_{\gamma\gamma}(\varepsilon)\approx(\ell_s/10)\,(\varepsilon\varepsilon_s)^{-1}$. Thus, if $\ell_s>10$ the source is opaque at $\varepsilon>\varepsilon_s^{-1}$ but due to the Klein–Nishina decline of the cross-section the source becomes transparent again at $\varepsilon>(\ell_s/10)\,\varepsilon_s^{-1}$. For $\varepsilon_s^{-1}<\gamma_{max}<(\ell_s/10)\,\varepsilon_s^{-1}$ the pair cascade is saturated until the mean energy of the cascading pairs and photons reach ε_s^{-1}. For every single particle injected at γ_{max}, there is at this point approximately $\gamma_{max}/\varepsilon_s^{-1}=\gamma_{max}\varepsilon_s$ particles and photons in the shower (Aharonian, Kirillov-Ugryumov & Vardanian 1985) with about ⅔ being electrons and positrons. The pair yield of this Klein–Nishina part of the cascade is then $x=\gamma_{max}\varepsilon_s/\gamma_{max}=\varepsilon_s$. The fate of the cascade below energies of ε_s^{-1} depends on whether ℓ_i is larger or smaller than about a few. If ℓ_i is small then the cascade stops and the pairs simply cool on the soft photons at ε_s making $N(\gamma)\propto\gamma^{-2}$ and $\alpha_{2-10}=\frac{1}{2}$. If ℓ_i is larger than a few then the cascade continues below ε_s^{-1} with the pair production taking place on the cascade photons in the X-rays. This Thomson part of the cascade is equivalent to the Thomson cascades treated in the present paper but with $\gamma_{max}\varepsilon_s\dot{N}$ particles of total power $(\frac{2}{3})\ell_i$ being 'injected' at $\approx\varepsilon_s^{-1}$. The number of Thomson generations is three or four and α_{2-10} and ℓ_{2-10} is expected to behave in the same way as for the case $\gamma_{max}=2.7\times10^4(\approx\varepsilon_s^{-1})$, discussed throughout this paper. The contours in Figs 12 and 13 would then become vertical in the Klein–Nishina region. The pair yield would be constant ($\approx\varepsilon_s$) at ℓ_i less than a few and is expected to join the $\gamma_{max}=2.7\times10^4$-curve in Fig. 8 at larger ℓ_i. There is most likely no pair gap in the pair yield curve at any γ_{max}.

7.2 HIGHER ORDER COMPTON CASCADES ($L_i>L_s$)

When $L_i>L_s$ then higher order Compton scatterings can no longer be neglected (Section 4.4.5 and Fig. 11). The X-ray spectrum will harden making a spectral slope, α_{2-10}, smaller than ½ possible (Zdziarski & Lamb 1986). For $L_i\gg L_s$ the particles no longer cool on the soft photons at ε_s but only on the dominant X-ray photons. As the X-ray photons completely dominate the radiation energy density, the Compton temperature *and* the thermal Comptonization effects that cooled secondary pairs have on the X-ray spectrum must be determined self-consistently.

The results from first-order Compton cascades do not easily carry over to higher order Compton cascades. Detailed calculations are needed.

8 Conclusions

We have attempted using largely analytical means to reach a partial understanding of pair cascades occurring in compact soft radiation fields. The main results are:

(i) Exact analytical solutions were found for the pair and photon injection spectra in saturated cascades. Each cascade generation has a unique spectral shape dependent only upon the primary particle injection spectrum. The first and second photon generations have characteristic spectral indices, $\alpha_1=½$ and $\alpha_2=¾$, respectively. The actual observed X-ray index, α_{2-10}, depends on the degree of overlap between the generations (determined by the value of $\gamma_{\max}\varepsilon_s$) and on the amount of further reprocessing due to down-scatter on the cooled thermal pairs (determined by ℓ_i). The saturated pair yield is easily evaluated and is of the order of 10 per cent at $\varepsilon_{\max,1}\gg 2$ having a maximum of 25 per cent at $\varepsilon_{\max,1}=8$.

(ii) Approximate analytical solutions were found for the pair and photon injection spectra in one-generation Thomson 'cascades' at any level of saturation (i.e. covering all values of ℓ_i) in the case when $\varepsilon_{\max,1}\varepsilon_{\max,2}<1$. The pair yield behaves linearly with ℓ_i at $\ell_i\ll 40$ and saturates to a constant value for large ℓ_i.

(iii) Opacity and pair-production feedbacks were identified as the cause for the change with increasing $\gamma_{\max}$ of the behaviour of the transition from unsaturated to saturated cascades. Approximate considerations of the pair injection rate at the Lorentz factor $\varepsilon_s^{-1/3}$ showed how these feedbacks operate. When $\gamma_{\max}$ becomes of the order of ε_s^{-1} the transition occurring at $\ell_i\approx 6$ is very sharp.

(iv) The emerging photon spectra from pair cascading clouds were determined by applying modifying radiative transfer factors to the injected photon spectra. Spectral breaks occur when ℓ_i is large at $\varepsilon=\tau_T^{-2}$ (due to down-scatter) and at $\varepsilon\approx$ a few (due to photon–photon absorption).

(v) The parameter space ($\gamma_{\max}$, ℓ_i) was investigated for the behaviour of α_{2-10} and ℓ_{2-10}. Observed values of $\alpha_{2-10}>½$ and ℓ_{2-10} occur in the unsaturated region $3\lesssim\ell_i\lesssim 10$, while $\alpha_{2-10}<½$ cannot be accounted for.

This investigation into the physics of pair cascades only covered part of parameter space and some very crude approximations had to be made. The resulting cascade models were neither final nor complete. Important observations with constraining power, e.g. the X-ray polarization or the spectral shapes and luminosities above say 20 keV and in the EUV band, are also lacking. It is therefore difficult at this stage to use the presented models to make any firm statement about the conditions in the X- and γ-ray emitting regions in compact objects.

Acknowledgments

The author thanks Clas-Ingvar Björnsson, Andy C. Fabian, Andrzej A. Zdziarski and, in particular, Gabriele Ghisellini for valuable discussions. A. A. Zdziarski, furthermore, provided many useful comments on the manuscript. A friendly HP75C pocket computer with 16kb of RAM was never down and supplied the necessary computing power.

References

Aharonian, F. A. & Vardanian, V. V., 1985. *Astrophys. Space Sci.*, **115,** 31.

Aharonian, F. A., Kirillov-Ugryumov, V. G. & Vardanian, V. V., 1985. *Astrophys. Space Sci.*, **115,** 201.

Aharonian, F. A., Vardanian, V. V. & Kirillov-Ugryumov, V. G., 1984. *Astrophys.* **20,** 118.

Barr, P., 1986. In: *Proceedings of Workshop on Variability in Galactic and Extragalactic X-ray Sources*, Como, Italy, in press.

Barr, P. & Mushotzky, R. F., 1986. *Nature,* **320,** 421.

Bassani, L. & Dean, A. J., 1983. *Space Sci. Rev.*, **35,** 367.

Bassani, L., Dean, A. J., Di Cocco, G. & Perotti, F., 1985. In: *Active Galactic Nuclei*, p. 252, ed. Dyson, J. E., Manchester University Press.

Beall, J. H., Wood, K. S. & Yentis, D. J., 1986. *Astrophys. J.,* **308,** 563.
Begelman, M. C., Blandford, R. D. & Rees, M. J., 1984. *Rev. Mod. Phys.,* **56,** 255.
Bezler, M., Kendziorro, E., Staubert, R., Hasinger, G., Pietsch, W., Reppin, C., Trümper, J. & Voges, W., 1984. *Astr. Astrophys.,* **136,** 351.
Bonometto, S. & Rees, M. J., 1971. *Mon. Not. R. astr. Soc.,* **152,** 21.
Brown, R. W., Mikaelian, K. O. & Gould, R. J., 1973. *Astrophys. Lett.,* **14,** 203.
Burns, M. L. & Lovelace, R. V. E., 1982. *Astrophys. J.,* **262,** 87.
Cavaliére, A., 1982. In: *Plasma Astrophysics*, p. 97, eds Gueynne, T. D. & Lévy, G., ESA SP-161, European Space Agency, Paris.
Cavaliére, A. & Morrison, P., 1980. *Astrophys. J.,* **238,** L63.
Crannell, C. J., Joyce, G., Ramaty, R. & Werntz, C., 1976. *Astrophys. J.,* **210,** 582.
Edelson, R. A. & Malkan, M. A., 1986. *Astrophys. J.,* **308,** 59.
Elvis, M., Green, R. E., Bechtold, J., Schmidt, M., Neugebauer, G., Soifer, B. T., Matthews, K. & Fabbiano, G., 1986. *Astrophys. J.,* **310,** 291.
Elvis, M. & Lawrence, A., 1985. In: *Astrophysics of Active Galaxies and Quasistellar Objects*, p. 289, ed. Miller, J. S., University Science Books, Mill Valley, USA.
Fabian, A. C., 1987. In: *The Physics of Accretion onto Compact Objects*, p. 229, eds Mason, K. O., Watson, M. G. & White, N. E., Springer-Verlag, Berlin.
Fabian, A. C., Blandford, R. D., Guilbert, P. W., Phinney, E. S. & Cuellar, L., 1986. *Mon. Not. R. astr. Soc.,* **221,** 931 (F86).
Ghisellini, G., 1987. *Mon. Not. R. astr. Soc.,* **224,** 1.
Gould, R. J. & Schréder, G. P., 1967. *Phys. Rev.,* **155,** 1404.
Guilbert, P. W., Fabian, A. C. & Rees, M. J., 1983. *Mon. Not. R. astr. Soc.,* **205,** 593.
Herterich, K., 1974. *Nature,* **250,** 311.
Jauch, J. M. & Rohrlich, F., 1976. *The Theory of Photons and Electrons,* 2nd edn, Springer-Verlag, New York.
Jelley, J. V., 1966. *Nature,* **211,** 472.
Kardashev, N. S., Novikov, I. D. & Stern, B. E., 1986. In: *IAU Symp. No. 119, Quasars,* p. 383, eds Swarup, G. & Kapahi, V. K., Reidel, Dordrecht, Holland.
Kazanas, D., 1984. *Astrophys. J.,* **287,** 112.
Landau, L. D. & Lifschitz, E. M., 1977. *Quantum Mechanics*, 3rd edn, Pergamon Press, Oxford.
Lightman, A. P. & Zdziarski, A. A., 1987. *Astrophys. J.,* in press.
Lovelace, R. V. E. & Ruchti, C. B., 1983. *Am. Inst. Phys. Conf. Proc.,* **101,** 314.
Novikov, I. D. & Stern, B. E., 1986. In: *Structure and Evolution of Active Galactic Nuclei,* p. 149, eds Giuricin, G. *et al.*, Reidel, Dordrecht, Holland.
Ore, A. & Powell, J. L., 1949. *Phys. Rev.,* **75,** 1696.
Osterbrock, D. E., 1974. *Astrophysics of Gaseous Nebulae*. W. H. Freeman & Co., San Francisco.
Perola, M. V., Piro, L., Altamore, A., Fiore, F., Boksenberg, A., Penston, M. V., Snijders, M. A. J., Bromage, G. E., Clavel, J., Elvius, A. & Ulrich, M. H., 1986. *Astrophys. J.,* **306,** 508.
Phinney, E. S., 1983. *PhD thesis*, University of Cambridge.
Rees, M. J., 1984. *Ann. Rev. Astr. Astrophys.,* **22,** 471.
Rothschild, R. E., Mushotzky, R. F., Baity, W. A., Gruber, D. E., Matteson, J. L. & Peterson, L. E., 1983. *Astrophys. J.,* **269,** 423.
Stern, B. E., 1985. *Sov. Astr.,* **29,** 306.
Sunyaev, R. A. & Titarchuk, L. G., 1980. *Astr. Astrophys.,* **86,** 121.
Svensson, R., 1982. *Astrophys. J.,* **258,** 321.
Svensson, R., 1983. *Astrophys. J.,* **270,** 300.
Svensson, R., 1986. In: *Radiation-Hydrodynamics in Stars and Compact Objects, IAU Coll. No. 89*, p. 325, eds Mihalas, D. & Winkler, K.-H. A., Springer-Verlag, Berlin.
Zdziarski, A. A., 1986. *Astrophys. J.,* **305,** 45.
Zdziarski, A. A. & Lamb, D. Q., 1986. *Astrophys. J.,* **309,** L79.
Zdziarski, A. A. & Lightman, A. P., 1985. *Astrophys. J.,* **294,** L79 (ZL85).

Appendix A: The photon kinetic equation

Consider equation (2.10) at photon energies $\varepsilon > 1$. The second and third term describing thermal Compton scatterings and photon–photon absorption are given by

$$\dot{n}_C^T(\varepsilon) = -ca_C(\varepsilon)\, n(\varepsilon) \tag{A1}$$

and

$$\dot{n}_{\gamma\gamma}(\varepsilon) = -ca_{\gamma\gamma}(\varepsilon)\, n(\varepsilon), \tag{A2}$$

where $a_C(\varepsilon)$ is the Compton scattering coefficient and $a_{\gamma\gamma}(\varepsilon)$ is the photon–photon absorption coefficient. Here $\dot{n}_C^T(\varepsilon)$ is viewed as a pure absorption term, i.e. the down-scattered photons with final energies >1 are neglected as a source term.

The radiative transfer equation (2.10) can now be solved in, e.g. uniform slab geometry, and the mean escape probability (neglecting all angular effects) becomes

$$\mathscr{E}(\varepsilon) = \frac{1-\exp[-\tau_{abs}(\varepsilon)]}{\tau_{abs}(\varepsilon)}, \tag{A3}$$

where the total absorption coefficient is

$$\tau_{abs}(\varepsilon) = R[a_C(\varepsilon) + a_{\gamma\gamma}(\varepsilon)]. \tag{A4}$$

For other geometries the expression for $\mathscr{E}(\varepsilon)$ will differ. For uniform spherical clouds $\mathscr{E}(\varepsilon)$ has the same limiting behaviour at large and small τ_{abs} apart from constants of order unity (e.g. Osterbrock 1974).

Replacing the radiative transfer term in equation (2.10) with a mean escape probability term gives

$$c\,\frac{dn(\varepsilon)}{ds} \approx \dot{n}_C^{NT}(\varepsilon)\,\mathscr{E}(\varepsilon). \tag{A5}$$

Equation (2.10) can then be solved for the photon density using equations (A1), (A2), and (A5) giving

$$n(\varepsilon) = \frac{\dot{n}_C^{NT}(\varepsilon)}{ca_{abs}(\varepsilon)}[1-\mathscr{E}(\varepsilon)]. \tag{A6}$$

The photon–photon absorption term, equation (A2), becomes using equation (A6)

$$\dot{n}_{\gamma\gamma}(\varepsilon) = -\dot{n}_C^{NT}(\varepsilon)[1-\mathscr{E}(\varepsilon)]\,\frac{a_{\gamma\gamma}(\varepsilon)}{a_{abs}(\varepsilon)}, \tag{A7}$$

which is our final form of the photon kinetic (and radiative transfer) equation.

Appendix B: Non-thermal processes

The non-thermal pair cascade is mediated by two processes: inverse Compton scattering and photon–photon pair production.

B.1 INVERSE COMPTON SCATTERING ($\gamma e \rightarrow \gamma e$)

The δ-function approximation of the differential cross-section is adopted,

$$\frac{d\sigma_T}{d\varepsilon}(\gamma, \varepsilon_s) = \sigma_T \delta(\varepsilon - \tfrac{4}{3}\gamma^2\varepsilon_s)\,\Theta(1-\tfrac{4}{3}\gamma\varepsilon_s), \tag{B1}$$

where ε_s, ε are the initial and final photon energies, respectively, and γ is the particle Lorentz factor. The step function Θ very roughly accounts for the Klein–Nishina decline of the cross-section.

The production rate of inverse Compton scattered photons at photon energy ε caused by a non-thermal electron (and positron) distribution, $N(\gamma)\,\mathrm{cm}^{-3}$, scattering soft photons with energy ε_s and number density n_s is

$$\dot{n}_C^{NT}(\varepsilon)=n_s c\int d\gamma\,\frac{d\sigma_T}{d\varepsilon}(\gamma,\varepsilon_s)\,N(\gamma)=n_s c\sigma_T\tfrac{3}{8}\varepsilon_s^{-1}\gamma^{-1}N(\gamma), \tag{B2}$$

where $\gamma=(3\varepsilon/4\varepsilon_s)^{1/2}$.

B.2 PHOTON–PHOTON PAIR PRODUCTION ($\gamma\gamma\rightarrow e^+e^-$)

The absorption coefficient $a_{\gamma\gamma}(\varepsilon)\,\mathrm{cm}^{-1}$ at photon energy ε in a radiation field with a power law spectral photon density $n(\varepsilon)\propto\varepsilon^{-(\alpha+1)}$ is given by (rewriting the results of Gould & Schréder 1967)

$$a_{\gamma\gamma}(\varepsilon)=\eta(\alpha)\,\sigma_T\,\frac{1}{\varepsilon}n\left(\frac{1}{\varepsilon}\right)=\eta(\alpha)\sigma_T\frac{E(1/\varepsilon)}{mc^2}\qquad(\alpha>-1), \tag{B3}$$

where

$$\eta(\alpha)=\tfrac{3}{8}\int_0^\infty ds_0 s_0^{-3-\alpha}\phi(s_0), \tag{B4}$$

where $E(\varepsilon)\,d\varepsilon$ is the radiation energy density in the interval $d\varepsilon$, and where $\phi(s_0)$ is proportional to the angle-averaged cross-section (Gould & Schréder 1967, corrections in Brown, Mikaelian & Gould 1973). Gould & Schréder (1967) calculated $\eta(\alpha)$ numerically for $\alpha=0$, 0.5, 1, and 1.5. Various approximations for $\eta(\alpha)$ have been used in the literature. The exact analytical expression for $\eta(\alpha)$ is (Svensson 1987, in preparation)

$$\eta(\alpha)=4^\alpha 6\,\frac{\Gamma^2(1+\alpha)}{\Gamma(5+2\alpha)}\,\frac{14+20\alpha+9\alpha^2+\alpha^3}{(3+\alpha)(2+\alpha)}\qquad(\alpha>-1), \tag{B5}$$

where $\Gamma(x)$ is the gamma function. Evaluating $\eta(\alpha)$ for integer and half-integer values of α gives 7/12, $211\pi/2800$, 11/90, $1623\pi/70560$, and 7/150 for $\alpha=0$, 0.5, 1, 1.5, and 2, respectively. A useful and very accurate approximation with an error of less than 0.3 per cent in the range $0<\alpha<6$ is

$$\eta(\alpha)=\tfrac{7}{6}(2+\alpha)^{-1}(1+\alpha)^{-5/3}. \tag{B6}$$

When the spectral slope of the radiation field depends weakly on the photon energy, then the absorption coefficient is approximately given by

$$a_{\gamma\gamma}(\varepsilon)\approx\eta[\alpha(1/\varepsilon)]\,\sigma_T\varepsilon^{-1}n(1/\varepsilon), \tag{B7}$$

i.e. $\eta(\alpha)$ is evaluated using the local slope at the threshold energy of the target photons.

As $\eta(\alpha)=0.24$, 0.12, 0.046 for $\alpha=0.5$, 1, and 2, respectively (the range of interest in our calculations) and as the largest dependence in $a_{\gamma\gamma}(\varepsilon)$ enters when $\alpha=0.5$ the value $\eta=0.2$ is used throughout.

The particles produced, when γ-ray photons of energy $\varepsilon\gg1$ interact with photons of energy $\varepsilon_1\ll\varepsilon$, have a mean Lorentz factor $\gamma=(\gamma_+ +\gamma_-)/2=(\varepsilon+\varepsilon_1)/2\approx\varepsilon/2$ and the production spectrum of particles is symmetric around the mean Lorentz factor. When the target radiation field has a power law distribution above the threshold $1/\varepsilon$ with spectral index $\alpha>-1$ then Bonometto & Rees (1971) showed by numerically integrating the rate that the production spectrum of particles *peaks* at $\gamma=\varepsilon/2$ for $\alpha\gtrsim0.6$. Indeed, Svensson (1987, in preparation) shows that the normalized

production spectrum (by number) is given by

$$K(\varepsilon, \gamma_+)=\frac{1}{\varepsilon}\frac{3}{8}\frac{(4E_*)^\alpha}{\eta(\alpha)}\left\{\left[\frac{4}{3+\alpha}-\frac{2}{2+\alpha}+\frac{4}{(2+\alpha)^2}-\frac{2}{1+\alpha}\right]4E_*+4\left[\frac{1}{1+\alpha}-\frac{1}{2+\alpha}\right]\right\}$$
$$(\varepsilon\gg 1, \alpha>-1), \tag{B8}$$

where $E_*=\gamma_-\gamma_+/\varepsilon^2=(1-\gamma_+/\varepsilon)\gamma_+/\varepsilon$. E_* peaks at $\gamma_+=\varepsilon/2$, and so does $K(\varepsilon, \gamma_+)$ for $\alpha>0.49$. A δ-function approximation where all particles emerge at $\gamma=\varepsilon/2$ does not introduce large errors, especially if in the end a broad-band distribution of γ-ray photons is integrated over.

The differential cross-section for photon–photon pair production, where a photon of energy ε interacts with a target photon of energy ε_1 to produce two particles at the energy $\gamma_+=\gamma_-$, is approximated by

$$\frac{d\sigma_{\gamma\gamma}}{d\gamma_+ d\varepsilon_1}(\varepsilon)=\eta(\alpha)\varepsilon_1\sigma_T\delta(\tfrac{1}{2}\varepsilon-\gamma_+)\,\delta\left(\frac{1}{\varepsilon}-\varepsilon_1\right), \tag{B9}$$

which correctly reproduces equation (B3) when integrated over. The factor $\eta(\alpha)\varepsilon_1$ can be interpreted as the effective bandwidth of target photons near threshold $1/\varepsilon$ that interact with incoming photons at ε with a cross-section σ_T. For steeper target spectra (increasing α) the bandwidth decreases rapidly.

Appendix C: Thermal processes

The two dominant thermal processes in this work are pair annihilation and Compton scattering. Here the annihilation rates are summarized.

C.1 DIRECT TWO PHOTON PAIR ANNIHILATION ($e^+e^-\rightarrow\gamma\gamma$)

The thermal pair annihilation rate in the Born approximation is only valid near $T\sim 10^8$ K. At larger temperature the Klein–Nishina corrections are important and at smaller temperatues Coulomb corrections become dominant. The annihilation rate is written as

$$\frac{dn_+}{dt}=n_+n_-cr_e^2\pi f_a(\theta) \qquad \text{cm}^{-3}\,\text{s}^{-1}, \tag{C1}$$

where $\theta\equiv kT/mc^2$ and where

$$f_a(\theta)=f_C(\theta)f_{KN}(\theta) \tag{C2}$$

is the total correction factor. The Coulomb correction is given by the fit

$$f_C(\theta)=[1+0.5(4\pi\alpha_f^2/\theta)^{0.6}+4\pi\alpha_f^2/\theta]^{1/2}, \tag{C3}$$

which deviates by at most 3 per cent from the exact non-relativistic cross-section (e.g. Landau & Lifschitz 1977) averaged over the Maxwell–Boltzmann distribution. α_f is the fine structure constant. The Klein–Nishina correction is

$$f_{KN}(\theta)=[1+2\theta^2/\ln(1.12\theta+1.3)]^{-1} \tag{C4}$$

to within 2 per cent (Svensson 1982).

C.2 TWO AND THREE PHOTON PAIR ANNIHILATION THROUGH POSITRONIUM FORMATION ($e^+e^-\rightarrow {}^1Ps\rightarrow\gamma\gamma$ or $e^+e^-\rightarrow {}^3Ps\rightarrow\gamma\gamma\gamma$)

The annihilation rate is determined by and is equal to the positronium formation rate as the

annihilation is prompt ($t_{2\gamma}\approx10^{-10}$ s and $t_{3\gamma}\approx1.4\times10^{-7}$ s) as compared to the positronium formation [$t_{ps}\approx R/(c\tau_T f_{ps})\approx300R_{13}/\tau_T f_{ps}$ s; for f_{ps} see below].

The indirect annihilation rate can be written

$$\frac{dn_+}{dt}=n_+n_-c\pi r_e^2 f_{ps}(\theta) \tag{C5}$$

with

$$f_{ps}(\theta)=3\times10^{-4}\theta^{-1} \qquad (3\times10^{-6}<\theta<5\times10^{-4}) \tag{C6}$$

which agrees with fig. 1 in Crannell *et al.* (1976) to within 15 per cent. The total annihilation rate becomes

$$\frac{dn_+}{dt}=n_+n_-c\pi r_e^2 g_a(\theta), \tag{C7}$$

where

$$g_a(\theta)=f_a(\theta)+f_{ps}(\theta). \tag{C8}$$

One quarter of the positronium annihilation events result in two photons with approximately the same spectrum as the free annihilation spectrum. The remaining three quarters of the events result in three photons with the approximate spectral emissivity (for $\theta\ll1$) given by

$$\varepsilon\dot{n}_{3\gamma}(\varepsilon)\approx n_+n_-cr_e^2\pi\tfrac{3}{4}f_{ps}(\theta)\varepsilon \qquad (\theta\ll\varepsilon<1) \tag{C9}$$

which deviates by no more than 15 per cent from the exact spectrum obtained by Ore & Powell (1949).

Appendix D: Analytical solutions for saturated pair cascades

Saturated pair cascades are described by the cascade functions $S_k(z)$ and $T_k(y_k)$. The kth generation of particle and photon injection is given by

$$\gamma^2P_k(\gamma)=\dot{N}\gamma^2S_k(z=\tfrac{2}{3}\gamma\varepsilon_s)=\dot{N}\gamma_{max}T_k(y_k) \quad \text{cm}^{-3}\,\text{s}^{-1} \tag{D1}$$

and by

$$\varepsilon^2\dot{n}_k(\varepsilon)=\tfrac{1}{4}\dot{N}\varepsilon^2S_k(z=\tfrac{1}{3}\varepsilon\varepsilon_s)=\dot{N}\gamma_{max}T_k(y_k) \quad \text{cm}^{-3}\,\text{s}^{-1}, \tag{D2}$$

respectively. Here, $\dot{N}\,\text{cm}^{-3}\,\text{s}^{-1}$ is a constant related to the particle injection rate, while y_k is defined by equation (3.11). The range for the kth pair generation is

$$\frac{\varepsilon_{min}}{2}<\gamma<\gamma_{max,k} \qquad \text{or} \qquad z_m<z<z_T^{2^k} \tag{D3}$$

and for the kth photon generation

$$\tfrac{1}{3}\varepsilon_{min}^2\varepsilon_s<\varepsilon<\varepsilon_{max,k} \quad \text{or} \quad z_m^2<z<z_T^{2^k}, \tag{D4}$$

where z_T and z_m are defined by equations (3.7) and (3.16), respectively.

D.1 MONO-ENERGETIC PARTICLE INJECTION

For mono-energetic injection $Q(\gamma)=\dot{N}\delta(\gamma-\gamma_{max})$ the cascade function for the kth generation is

described by (dropping the subscript on y)

$$T_k(y)=\frac{1}{2}\sum_{j=1}^{k} q_k^j y^{2^{-(k+1-j)}}, \tag{D5}$$

where $q_{k+1}^j=\frac{1}{2}[1-2^{-(k+1-j)}]^{-1}q_k^j$, $q_{k+1}^{k+1}=-(2^k-1)^{-1}q_k^k$ (or use

$$\sum_{j=1}^{k} q_k^j=1$$

to determine q_k^k), and $q_1^1=1$.

The first generations become

$$T_1(y)=\tfrac{1}{2}y^{-1/2} \tag{D6a}$$

$$T_2(y)=\tfrac{1}{2}(y^{1/4}-y^{1/2}) \tag{D6b}$$

$$T_3(y)=\tfrac{1}{2}(\tfrac{2}{3}y^{1/8}-y^{1/4}+\tfrac{1}{3}y^{1/2}) \tag{D6c}$$

$$T_4(y)=\tfrac{1}{2}(\tfrac{8}{21}y^{1/16}-\tfrac{2}{3}y^{1/8}+\tfrac{1}{3}y^{1/4}-\tfrac{1}{21}y^{1/2}). \tag{D6d}$$

$T_k(y)$ has a maximum of value $\frac{1}{8}$, $(2\sqrt{3}-3)/8=0.058$, and 0.0286 at $y=(\frac{1}{2})^4$, $[(\sqrt{3}-1)/2]^8$, and $(0.3177)^{16}$ for $k=2$, 3, and 4, respectively. Note that the leading term of $T_k(y)$ for $y\ll 1$ is $\propto y^{1/2^k}$. The cascade functions for mono-energetic injection are shown as a function of y in Fig. 2 and as a function of z in Fig. 3(a) and (b) for $z_T=0.05$ and 0.5, respectively.

The local spectral index α_k of each generation is determined by

$$\alpha_k=1-\frac{d\ln T_k(y)}{d\ln y} \tag{D7}$$

which for the first three generations becomes

$$\alpha_1=\tfrac{1}{2} \tag{D8a}$$

$$\alpha_2=\tfrac{3}{4}+\tfrac{1}{4}\frac{u}{1-u} \tag{D8b}$$

$$\alpha_3=\tfrac{7}{8}+\tfrac{3}{8}\frac{u(1+u)}{(1-u)(2+u)} \tag{D8c}$$

where

$$u=y^{1/2^k}. \tag{D9}$$

D.2 POWER LAW PARTICLE INJECTION

For power law particle injection according to equation (3.22) and for ($\Gamma\neq 1$) the first few cascade functions becomes

$$T_1(y)=\tfrac{1}{2}\frac{1}{\Gamma-1}[y^{(2-\Gamma)/2}-y^{1/2}] \tag{D10a}$$

$$T_2(y)=\tfrac{1}{2}\frac{1}{\Gamma-1}\left[\frac{1}{\Gamma}y^{(2-\Gamma)/4}-y^{1/4}+\left(1-\frac{1}{\Gamma}\right)y^{1/2}\right] \qquad (\Gamma\neq 0) \tag{D10b}$$

$$T_3(y)=\tfrac{1}{2}\frac{1}{\Gamma-1}\left[\frac{2}{\Gamma(2+\Gamma)}y^{(2-\Gamma)/8}-\tfrac{2}{3}y^{1/8}+\left(1-\frac{1}{\Gamma}\right)y^{1/4}+\left(\frac{1}{2+\Gamma}-\tfrac{1}{3}\right)y^{1/2}\right] \qquad (\Gamma\neq -2,0). \tag{D10c}$$

The leading term of $T_k(y)$ for $\Gamma>1$ is $\propto y^{(2-\Gamma)2^{-k}}$, which approaches a constant for large k when $\Gamma\neq 2$, while always being constant when $\Gamma=2$. The leading term for $\Gamma<1$ is $\propto y^{2^{-k}}$, since the sign change of $(\Gamma-1)^{-1}$ makes the second term positive and dominant. The cascade functions for power law injection are shown in Fig. 5(a) and (b) for $z_T=0.5$ and for $\Gamma=1.2$ and 2, respectively.

Appendix E: Second-order Compton scattering

The photon injection rate due to photons scattering a second time is determined by

$$\dot{n}_{C2}^{NT}(\varepsilon)=c\int\int N(\gamma)n_{C1}^{NT}(\varepsilon)\,\frac{d\sigma_T}{d\varepsilon}(\gamma,\varepsilon_1)\,d\varepsilon_1\,d\gamma, \tag{E1}$$

where the spectral photon density of first-order photons is given by equations (2.22) and (2.23) as

$$n_{C1}^{NT}(\varepsilon)=\frac{R_i}{c}\dot{n}_C^{NT}(\varepsilon)\,\mathscr{E}(\varepsilon). \tag{E2}$$

Here R_i is the radius of the particle injection region (denoted by R elsewhere). Equation (E2) is used only for $\varepsilon<1$ as photons with $\varepsilon>1$ scatters in the Klein–Nishina limit and are thus neglected here (see equation B1). Equation (2.12) can be used for $N(\gamma)$ as long as the particles cool mainly on the soft photons at ε_s. Using equations (2.12), (2.13), (B1) and (E2) and performing the ε_1-integration in equation (E1) gives

$$\frac{\dot{n}_{C2}^{NT}(\varepsilon)}{\dot{N}}=\frac{R_i\dot{N}}{cn_s}\frac{3}{8}(\varepsilon\varepsilon_s)^{-3/2}\int_{\gamma_{low}}^{\gamma_{up}}\frac{1}{\gamma}\mathscr{E}\left(\frac{3\varepsilon}{4\gamma^2}\right)$$
$$\times\int_{\gamma}^{\gamma_{max}}\frac{[Q(\gamma')+P(\gamma')]}{\dot{N}}d\gamma'\int_{\gamma''_{low}}^{\gamma_{max}}\frac{[Q(\gamma'')+P(\gamma'')]}{\dot{N}}d\gamma''\,d\gamma,$$

where

$$\gamma_{up}=\min\left[\gamma_{max},\ \frac{3}{4}\left(\frac{\varepsilon}{\varepsilon_s}\right)^{1/2}\right],\qquad \gamma_{low}=\max\left[1,\ \frac{3}{4\gamma_{max}}\left(\frac{\varepsilon}{\varepsilon_s}\right)^{1/2},\varepsilon\right], \tag{E4}$$

and

$$\gamma''_{low}=\max\left[1,\ \frac{3}{4\gamma}\left(\frac{\varepsilon}{\varepsilon_s}\right)^{1/2}\right]. \tag{E5}$$

Neglecting down-scattering, i.e. setting $\mathscr{E}(\varepsilon)=1+\tau_T/3$, overestimates the second-order injection but has the virtues of making the calculations analytically tractable and of giving upper limits to the second-order contribution. For mono-energetic injection (equation 3.15) the photon injection rate becomes

$$\frac{\dot{n}_{C2}^{NT}(\varepsilon)}{\dot{N}}=\frac{\ell_i}{\ell_s}\frac{R_s}{R_i}\frac{\varepsilon_s}{\gamma_{max}}\int_{\gamma_{low}}^{\gamma_{up}}\frac{1}{\gamma}\left[1+\int_{\gamma}^{\gamma_{max,1}}\frac{P(\gamma')}{\dot{N}}d\gamma'\right]\left[1+\int_{\gamma''_{low}}^{\gamma_{max,1}}\frac{P(\gamma'')}{\dot{N}}d\gamma''\right]d\gamma, \tag{E6}$$

where

$$\frac{R_i\dot{N}}{cn_s}\mathscr{E}(\varepsilon)\approx\frac{L_i}{L_s}\left(\frac{R_s}{R_i}\right)^2\frac{\varepsilon_s}{\gamma_{max}}=\left(\frac{\ell_i}{\ell_s}\frac{R_s}{R_i}\right)\frac{\varepsilon_s}{\gamma_{max}} \tag{E7}$$

has been used and where R_s is the size of the region where soft photons are injected.

Let $\dot{n}_{km}(\varepsilon)$ represent the injection rate of photons that have scattered, first on the kth pair generation and then on the mth pair generation. Denoting the injected particles as the 0th

generation the indices k and m run from 0 to K. The total injection rate is then

$$\dot{n}_{C2}^{NT}(\varepsilon)=\sum_{k=0}^{K}\sum_{m=0}^{K}\dot{n}_{km}(\varepsilon) \tag{E8}$$

consisting of $(K+1)^2$ terms. Defining

$$z=\tfrac{2}{3}\gamma\varepsilon_s, \qquad y_k=\frac{z}{z_T^{2^k}}, \tag{E9a}$$

and

$$g=\frac{\varepsilon_s}{3}(\varepsilon\varepsilon_s)^{1/2}, \qquad g_k=\frac{g}{z_T^{2^k}}=\left(\frac{\varepsilon_s}{\varepsilon}\right)^{1/2}\frac{\varepsilon}{\varepsilon_{\max,k}} \tag{E9b}$$

and using equation (D1) makes it possible to write the terms $\dot{n}_{km}(\varepsilon)$ in a simple form. There are four types of terms:

$$\varepsilon^2\frac{\dot{n}_{00}(\varepsilon)}{\dot{N}}=\gamma_{\max}\left(\frac{\ell_i}{\ell_s}\frac{R_s}{R_i}\right)\tfrac{1}{2}g_2\int\frac{dz}{z}, \tag{E10}$$

$$\varepsilon^2\frac{\dot{n}_{0m}(\varepsilon)}{\dot{N}}=\gamma_{\max}\left(\frac{\ell_i}{\ell_s}\frac{R_s}{R_i}\right)\frac{1}{2z_T}g_k\int 2y_m^{-2}T_{m+1}(y_m^2)\,dy_m \qquad (m\neq 0), \tag{E11}$$

$$\varepsilon^2\frac{\dot{n}_{k0}(\varepsilon)}{\dot{N}}=\gamma_{\max}\left(\frac{\ell_i}{\ell_s}\frac{R_s}{R_i}\right)\frac{1}{2z_T}\int 2T_{k+1}(g^2z^{-2}z_T^{-2^{k+1}})\,dz \qquad (k\neq 0). \tag{E12a}$$

Lastly, for photons scattering twice on secondary pairs

$$\varepsilon^2\frac{\dot{n}_{km}(\varepsilon)}{\dot{N}}=\gamma_{\max}\left(\frac{\ell_i}{\ell_s}\frac{R_s}{R_i}\right)\frac{1}{2}\int 4y_m^{-1}T_{k+1}(g_{k+m}^2y_m^{-2})\,T_{m+1}(y_m^2)\,dy_m \qquad (k,m\neq 0). \tag{E13}$$

The integration limits for arbitrary k and m are given by

$$z_{up}=\min[\tfrac{1}{2}(\varepsilon\varepsilon_s)^{1/2}, z_T^{2^m}]; \qquad z_{low}=\max[\tfrac{2}{3}\varepsilon_s, gz_T^{-2^k}, 2z] \tag{E14}$$

with the corresponding limits on the y_k- and y_m-integration obtainable from equation (E9a).

Equation (E12a) can be transformed into an expression identical to equation (E11) by making the substitutions $z'=g/z$ and $y_k=z'/z^{2k}$ giving

$$\varepsilon^2\frac{\dot{n}_{k0}(\varepsilon)}{\dot{N}}=\gamma_{\max}\left(\frac{\ell_i}{\ell_s}\frac{R_s}{R_i}\right)\frac{1}{2z_T}g_k\int 2y_k^{-2}T_{k+1}(y_k^2)\,dy_k \qquad (k\neq 0) \tag{E12b}$$

with integration limits

$$z'_{up}=\min[\tfrac{1}{2}(\varepsilon\varepsilon_s)^{1/2}, z_T^{2^k}, \tfrac{1}{2}gz^{-1}]; \qquad z'_{low}=\max[\tfrac{2}{3}\varepsilon_s, gz_T^{-1}]. \tag{E15}$$

The spectral range for arbitrary k and m is

$$\frac{16}{9}\varepsilon_s<\varepsilon<\min\left[\gamma_{\max,\,m},\ \frac{16}{9}\gamma_{\max,k}^2\gamma_{\max,m}^2\varepsilon_s,\ \frac{9}{16\varepsilon_s}\right]. \tag{E16}$$

For *saturated* pair production the cascade functions $T_k(y)$ are given by equations (D5) or (D6). It is straightforward to do the integrals. Fig. 11(a) and (b) show the saturated second-order Compton spectra for $\gamma_{\max}=3\times10^3$ and 2.7×10^4 with $\varepsilon_s=2.7\times10^{-5}$. As an example, the dominant term in Fig. 11(a) is simply

$$\varepsilon^2\frac{\dot{n}_{11}(\varepsilon)}{\dot{N}}=\gamma_{\max}\left(\frac{\ell_i}{\ell_s}\frac{R_s}{R_i}\right)\frac{1}{2}[(g_2+g_2^{1/2})\ln y_1-2g_2^{1/2}y_1^{1/2}+2g_2y_1^{1/2}]_{y_1(z_{low})}^{y_1(z_{up})}. \tag{E17}$$